Effectiveness of NAD+ in inhibiting senescent phenotypes of RPE cells to mitigate disease progression in mouse models of Age-Related Macular Degeneration

Gang Cui

The Graduate School
Yonsei University
Department of Medicine

Effectiveness of NAD+ in inhibiting senescent phenotypes of RPE cells to mitigate disease progression in mouse models of Age-Related Macular Degeneration

A Dissertation Submitted
to the Department of Medicine
and the Graduate School of Yonsei University
in partial fulfillment of the
requirements for the degree of
Doctor of Philosophy in Medical Science

Gang Cui

June 2024

This certifies that the Doctoral Dissertation of Gang Cui is approved.

[signature]

Thesis Supervisor Suk Ho Byeon

[signature]

Thesis Committee Member Hak-Joon Sung

[signature]

Thesis Committee Member Jeong Hun Bae

[signature]

Thesis Committee Member Ikhyun Jun

[signature]

Thesis Committee Member Junwon Lee

The Graduate School
Yonsei University
June 2024

ACKNOWLEDGEMENTS

I am profoundly grateful to the Yonsei University College of Medicine for presenting me with a precious learning opportunity. My doctoral studies and work have substantially improved my professional knowledge and learning capabilities. I am also thankful for the scholarship provided by the university, which significantly lightened my financial burden.

Special thanks to my Professor Suk Ho Byeon, for his care in my personal life and his professional guidance in my studies throughout my pursuit of a doctorate. I am equally thankful to my co-advisor, Professor Junwon Lee, for his substantial support in various aspects of my life, including studies, work, and research.

Thanks to Professors Hak-Joon Sung, Jeong Hun Bae, and Ikhyun Jun, who offered their help in the writing of papers related to my doctoral project. I am also deeply appreciative of Professor Jang-Ung Park from the Yonsei University Department of Materials Science, who involved me in a significant research project on artificial retinas, which was published in Nature Nanotechnology.

As an international student, the support from my colleagues at Yonsei University was indispensable for the successful completion of my doctoral studies. I want to thank Jinkyu Park, Han Jeong, Haesol Shin, Yoonjung Seo, Hyundong Lee, Minjae Ohn, Minseok

Choi, and Jeong Ah Lim for their encouragement and assistance in my daily life. A special thank you to Won Gi Chung, Sanghoon Lee, and Jiuk Jang from the Department of Materials Science. The days spent working on experiments with you will be unforgettable.

I am also grateful for my dear friends Zhen Xu, Hui Jin, Xiangzhe Li, Ying Cui, and Xianyu Wen, whose companionship was a driving force behind the successful completion of `my studies. Lastly, my deepest appreciation goes to my wife and my parents for their silent support, and to my lovely daughter.

After graduation, I intend to maintain close connections with my friends in Korea and to seek various opportunities for collaborative research.

TABLE OF CONTENTS

LIST OF FIGURES

ABSTRACT IN ENGLISH

Effectiveness of NAD+ in Inhibiting senescent phenotypes of RPE Cells to Mitigate Disease Progression in Mouse Models of Age-Related Macular Degeneration

Age-related macular degeneration (AMD) is the leading cause of blindness among the elderly in developed countries. AMD is categorized into dry and wet types; Dry AMD is characterized by retinal pigment epithelium (RPE) atrophy, lacking effective treatments. Wet AMD originates from choroidal neovascularization and is treated with repetitive intraocular injections of a monoclonal antibody targeting vascular endothelial growth factor (VEGF), nevertheless, long-term observation unveils the progression to subretinal fibrosis and deterioration of visual acuity, indicating unmet therapeutic needs [1]. With aging, intracellular levels of nicotinamide adenine dinucleotide (NAD+) in human decline, including in the retina [2]. Numerous studies have demonstrated the anti-aging effects and therapeutic benefits of raising NAD+ levels in age-related diseases. In this study, we investigated the therapeutic effects of NAD+ elevation in an in vivo model of dry and wet AMD.

In both the geographic atrophy (GA) model of advanced dry AMD and the laser-induced choroidal neovascularization (CNV) model of wet AMD, increased expression of senescence markers and decreased intracellular NAD+ levels were confirmed in the retina.

Systemic supplementation of the NAD+ precursors such as nicotinamide mononucleotide (NMN) and nicotinamide riboside (NR) resulted in an elevation of retinal NAD+ levels. In an in vivo GA model, NAD+ precursors significantly reduced RPE atrophy, decreased the expression of age-related markers, and improved visual function. Transcriptome analysis revealed that NAD+ precursors reduced inflammation-related gene set expression and increased visual system-related gene set expression. Additionally, NAD+ precursors led to a substantial reduction of the lesion size in the laser-induced CNV model, which was comparable to the current

clinical intervention of intravitreal aflibercept. The gene expression of aging markers, angiogenic factors, and senescence-associated secreting phenotype (SASP) was significantly reduced in the NAD+ precursor treated cases. Furthermore, this treatment strategy concurrently facilitated a decrease in subretinal fibrosis.

Clinical trials are currently underway to explore the efficacy of NAD+ precursors in treating various diseases and counteracting aging, and which are considered safe for use in humans. Based on the evidence from our preclinical models, supplementation with NAD+ precursors could be employed as a novel treatment approach for age-related macular degeneration, a disease with limited therapeutic options.

Key words :Age-related macular degeneration, Senescence, Nicotinamide Adenine Dinucleotide

I. INTRODUCTION

Age-related macular degeneration (AMD) is a retinal disorder predominantly affecting the macula, the central region of the retina, and is a leading cause of vision impairment among the elderly in developed countries [3]. AMD manifests primarily in two forms: dry (atrophic) and wet (neovascular or exudative) [4]. Currently, geographic atrophy (GA) of advanced dry AMD has no established treatment and has relied on nutritional supplements [5]. The strategy of complement cascade inhibition has been proposed as a novel approach for the treatment of GA, yet its clinical efficacy requires further validation [6]. While therapeutic approaches for choroidal neovascularization (CNV) of advanced wet AMD predominantly encompass anti-vascular endothelial growth factor (anti-VEGF) treatments [7]. Although current anti-VEGF strategy for wet AMD show promise in ameliorating the disease condition, the efficacy remains suboptimal and long-term observation unveils the progression to subretinal fibrosis and deterioration of visual acuity [1]. Therefore, there exists a significant unmet need in the treatment of macular degeneration, necessitating the exploration of novel mechanisms of action.

The pathogenesis of AMD is complex, characterized by the intricate interaction of genetic predispositions, environmental factors, and metabolic dysregulation [4,8-12]. Aging is most important risk factors and recent studies highlight the significance of senescence, where DNA damage and metabolic anomalies impair cellular functions, in the development of AMD [13-15]. Cellular senescence plays a critical role in various diseases, with the Senescence-associated Secretory Phenotype (SASP) comprising inflammatory mediators, extracellular matrix components, proteolytic enzymes, and growth factors secreted by senescent cells [15-20]. Also in the AMD, the cellular senescence exacerbates the pathological changes, driving the retinal degeneration and the disruption of tissue homeostasis, through pro-inflammatory SASP secreted by the senescent cells in the retina and choroid [21-23].

Given the contribution of cellular senescence to the progression of AMD, therapeutic strategies targeting cellular senescence have been explored. Current strategies can be divided into two main categories: senolytics, which focus on selectively eliminating senescent cells, and senomorphics, aiming to modulate the senescent phenotype without necessarily killing the cells [24]. Additionally, interventions to restore cell homeostasis represent another crucial approach, focusing on rejuvenating the cellular environment to prevent or delay senescence-related pathologies [25-27].

Metabolic dysregulation in photoreceptor or RPE cells is associated with blinding diseases such as Leber congenital amaurosis type 9, Leber hereditary optic neuropathy and Age-Related Macular Degeneration [28]. NAD+ is the central hydride-transferring cofactor in metabolism and a substrate for NAD+-consuming enzymes [29-31]. Maintaining NAD+ levels are critical to retinal health. Retinal NAD+ levels decrease with age in mice [32], decline with age-related disease conditions [54], diminished in several models of retinal degeneration [32-35], and are low in post mortem RPE from AMD patients [28]. Diminished activities of nicotinamide mononucleotide adenylyltransferase-1 or nicotinamide phosphoribosyl transferase, enzymes required for NAD+ biosynthesis, cause retinal dystrophy in humans and retinal degeneration in mice [31,32,36]. Conversely, treatment with NAD+ biosynthetic precursors nicotinamide or nicotinamide mononucleotide, protects against retinal degeneration in mice and rats [32,33].

NAD+ is a coenzyme found in all living cells. It serves both as a critical coenzyme for enzymes that fuel reduction-oxidation reactions and as a co-substrate for other enzymes such as the sirtuins and poly(adenosine diphosphate–ribose) polymerases. Cellular NAD+ concentrations change during aging, and modulation of NAD+ usage or production can prolong both health span and life span [37].

NAD+ is intracellular molecule functioning in maintaining cellular health and mitigating senescence [25]. A decline in NAD+ levels, characteristic of cellular senescence and prevalent in various age-related pathologies, is linked not only to a deficiency in NAD+ salvage pathways in aging and senescent cells [38] but also to increased consumption by enzymes such as CD38 and PARP1. CD38 and PARP1, particularly expressed in activated macrophages, and the heightened activity of these NAD+-consuming enzymes, especially during aging as DNA damage accumulates, further contribute to the depletion of NAD+ in these cells [25,37-41]. This reduction correlates with decreased energy production efficiency, impaired DNA repair, disrupted redox homeostasis, and amplified inflammatory responses [42-45]. Enhancement of NAD+ levels, for instance through supplementation with precursors like NMN and NR, is suggested as a potential intervention to augment cellular and tissue functions, potentially decelerating the senescence process [26,46-53].

In this study, within the broader context of therapeutic effects of NAD+ precursor supplements on age-related diseases, we explored the therapeutic effects of NAD+ precursor supplementation in an in vivo model of dry and wet AMD.

II. MATERIALS AND METHODS

1. Animal

Adult C57BL/6 J mice, aged 8– 10 weeks and weighing between 18– 20 grams, were utilized for this study. The C57BL/6 J mice were housed under a controlled 12:12- hour light/dark cycle throughout the study. Mice were maintained in accordance with the Association for Research in Vision and Ophthalmology (ARVO) Statement for the Use of Animals in Ophthalmic and Vision Research. All animal experiments were approved by the Institutional Animal Care and Use Committee (IACUC) of the Yonsei University College of Medicine (IACUC number: 2022–0279). All methods were conducted following the relevant guidelines and regulations, and the study is reported adhering to the ARRIVE guidelines.

2. NAD+ supplementation

Nicotinamide mononucleotide (NMN) (Oriental Yeast Co., Ltd., Japan) and nicotinamide riboside (NR) (ChromaDex, Inc., USA) powders were used in this study for NAD+ supplement. Both NMN and NR were dissolved in phosphate- buffered saline (PBS) to achieve a concentration of 200 mg/ml and subsequently filtered. Mice received intraperitoneal (IP) injections at a dose of 500 mg/kg NMN or NR. The administration of these injections began three days before the establishment of the disease models and continued daily until the final assessment. NMN and NR were stored as powders, with each injection solution freshly prepared and used within one week.

3. Sodium Iodate induced GA in the mouse model of AMD

We utilized sodium iodate (S4007; Sigma St. Louis, MO) powder, which was dissolved in phosphate- buffered saline (PBS) to achieve a concentration of 1 mg/ml. The solution was administered to the mice via tail vein injection at concentrations of 15, 20, and 25 mg/kg, respective to their body weight. Control group mice received an equivalent volume of PBS through the same method of administration.

4. Alu-RNA expressed Lenti-virus induced GA in the mouse model of AMD

A lentivirus expressing EGFP and Alu RNA was injected subretinally in mice at a concentration

of 8x10^7 particles in 1 μl, following the method outlined in our previously published study. Briefly, the lentivirus was diluted in phosphate- buffered saline (PBS) to a final concentration of 8x10^10 particles/ml. A volume of 1 μl of the virus was loaded into a microliter syringe equipped with a 34G needle and slowly injected into the subretinal space of the mice, ensuring no bleeding occurred during the injection and gently withdrawing the needle afterwards. Mice that did not exhibit significant vitreous hemorrhage or inflammatory reactions in the eyes post-procedure were selected for subsequent analysis.

5. Mouse model of laser-induced CNV and Subretinal Fibrosis

The Choroidal Neovascularization (CNV) mouse model was created using laser photocoagulation, similar to the method described in our previous publication [45]. Briefly, mice were anesthetized and their pupils were dilated. Once full dilation of the pupils was achieved, a 532 nm wavelength laser was employed with settings of 100 μm spot size, 150 mW power, and 100 ms exposure time. Three or four laser burns were positioned around the optic disc. Only burns that resulted in bubble formation without hemorrhage were included in the analysis. CNV-related assessments were conducted one-week post- model creation, and fibrosis- related analyses were performed four weeks after model establishment [46].

6. Mouse tissue preparation

For the preparation of tissues for RNA extraction, mice were euthanized using carbon dioxide inhalation following approved ethical guidelines. Subsequently, the eyeballs were enucleated and rinsed with cold phosphate- buffered saline (PBS). While immersed in cold PBS, the surrounding muscles, conjunctival tissue, and anterior segment parts, including the cornea, iris, and lens, were meticulously excised. The neural retina and RPE/choroid complex were then carefully isolated for subsequent RNA extraction.

For whole-mount tissue preparation, mice were euthanized as previously described, and their eyeballs were then enucleated and rinsed with phosphate- buffered saline (PBS). The tissues were then fixed in 1% paraformaldehyde (PFA) in PBS for one hour. Following fixation, the muscular and conjunctival tissues, cornea, iris, and lens were carefully removed from the eyeballs in PBS. The neural retina was separated and removed, leaving the RPE/choroid complex, which was then radially sectioned into eight segments centered around the optic disc, resembling a leaf pattern. These sectioned tissues were placed in microtubes containing PBS for

further analysis.

For cryosection preparation, mouse eye tissues were rinsed with phosphate- buffered saline (PBS) after enucleation. Surrounding muscles, conjunctiva, cornea, iris, and lens were then removed in PBS. Tissues were fixed for 30 minutes in a solution of 4% paraformaldehyde (PFA) and 5% sucrose in PBS, followed by sequential immersion in 10% and 20% sucrose solutions for approximately one hour each. Subsequently, tissues were placed in 30% sucrose in PBS overnight. The next day, tissues were embedded in OCT compound, set for one hour, and rapidly frozen in liquid nitrogen for storage at -80°C or immediate cryosectioning.

7. Cellular NAD+ measurement

NAD+ concentrations were determined using the NAD/NADH Assay Kit (ab65348, Abcam, Cambridge, UK). Tissues from the mouse neural retina and RPE/choroid complex, as well as iPSC- derived RPE cells, were homogenized in the kit's extraction buffer and then centrifuged at 10,000 g for 5 minutes at 4°C. The supernatants obtained were filtered using a 10 kDa Spin Column (ab93349, Abcam, Cambridge, UK). Total NADt levels were measured directly from the filtered supernatant. For the specific quantification of NAD+ levels, the supernatants were treated at 60°C for 30 minutes to decompose any NAD+. The NAD+ concentration was then determined by subtracting the amount of decomposed NADH from the total NADt in the supernatant.

8. RNA isolation and real-time PCR

To extract RNA from the prepared tissues, we employed the RNA extraction kit (R1013, ZYMO RESEARCH, CA, USA). The tissues were initially homogenized using the lysis buffer provided in the kit. This process was followed by a series of centrifugation steps to separate cellular debris. The supernatant containing RNA was then treated according to the protocol of the R1013 kit, which included an alcohol-based solution for RNA binding to the silica membrane of the spin columns included in the kit. After extensive washing steps to remove any impurities, the RNA was eluted in RNase-free water. Immediately following the RNA extraction, we commenced cDNA synthesis using the cDNA synthesis kit (SD2191, Takara, CA, USA), ensuring a streamlined transition from RNA extraction to cDNA preparation for downstream molecular analyses.

Following the synthesis of cDNA from the extracted, we proceeded with real-time quantitative

PCR (qPCR) analysis. The cDNA was used as a template for qPCR, which was performed using a real-time PCR kit (43-676-59, Fisher Scientific, MA, USA). Each reaction mixture included specific primers targeting our genes of interest, a SYBR Green PCR master mix from the kit, and an appropriate amount of template cDNA. The reactions were carried out in a real-time PCR system, starting with an initial denaturation step, followed by 40 cycles of denaturation, annealing, and extension. The specific temperatures and times for each step were set according to the kit's protocol. The relative expression levels of the target genes were determined by comparing their cycle threshold (Ct) values to those of a reference gene, using the 2^-ΔΔCt method for quantification.

Real-time qPCR was conducted using primers for: COL1 (FP:5'- ACGCCATCAAGGTCTACTGC- 3', RP:5'- ACTCGAACGGGAATCCATCG- 3'), IL- 1α (FP:5' -GTTCTGCCATTGACCATCTC- 3', RP:5'- CTCAGCCGTCTCTTCTTCAG- 3'), IL- 1β (FP:5'- TCCTTGTGCAAGTGTCTGAA- 3', RP:5'- CTCTTGTTGATGTGCTGCTG- 3'), IL- 6 (FP:5'- ACGGCCTTCCCTACTTCACA- 3', RP:5'- CATTTCCACGATTTCCCAGA- 3'), Mmp3 (FP:5'- TTGATGGGCCTGGAACAGTC- 3', RP:5'- AGTCCTGAGAGATTTGCGCC- 3'), Mmp13 (FP:5'- GGAGCCCTGATGTTTCCCAT- 3', RP:5'- GTCTTCATCGCCTGGACCATA- 3'), Cxcl1 (FP:5'- CTGGGATTCACCTCAAGAACATC- 3', RP:5'- CAGGGTCAAGGCAAGCCTC- 3'), Ccl2 (FP:5'- CATCCACGTGTTGGCTCA- 3', RP:5'- GATCATCTTGCTGGTGAATGAGT- 3'), PDGF- BB (FP:5'- TGTTCCAGATCTCGCGGAAC- 3', RP:5'- GCGGCCACACCAGGAAG- 3'), TGF- β (FP:5'- TTGCTTGAGCTCCACAGAGA- 3', RP:5'- TGGTTGTAGAGGGCAAGGAC- 3'), FGF- 2 (FP:5'- CCGCGTGGATGGCGT- 3', RP:5'- CCTCTCTCTTCTGCTTGGAGTTG- 3'), VEGF (FP:5'- AGCAGAAGTCCCATGAAGTG- 3', RP:5'- CATGGTGATGTTGCTCTCTG- 3').

9. Cryosection and hematoxylin and eosin staining

The OCT- embedded blocks were sectioned at a thickness of 7 μm. These sections were then stained with hematoxylin and eosin. All images were captured using a fluorescent upright microscope (Olympus; BX43).

10. Immunofluorescence of retinal sections and RPE/choroid/sclera complex

For immunofluorescence staining of eye tissue sections, cryosections were initially blocked in a

solution containing 2% normal donkey serum, 5% BSA, and 0.1% Triton X- 100 in PBS for one hour. Subsequently, the sections were incubated with the primary antibody overnight at 4°C. After rinsing, they were treated with the secondary antibody for one hour. The sections were then mounted using DAPI-containing mounting media.

For whole- mount immunofluorescence staining, tissues in microtubes were first incubated with 1% Triton X- 100 for two hours. They were then incubated for an additional hour in a solution containing 2% normal donkey serum, 5% BSA, and 0.1% Triton X- 100 in PBS. Subsequently, the tissues underwent overnight incubation with the primary antibody and a subsequent one-hour incubation with the secondary antibody. Finally, the tissues were flat-mounted on slides and covered with DAPI-containing mounting media.

In this experiment, the primary antibodies used include ZO- 1 (61-7300, Invitrogen, MA, USA), Isolectin B4(I121411, Invitrogen, MA, USA), Collagen type I(ab34710, Abcam, Cambridge, UK), P16INK4a (ab211542, Abcam, Cambridge, UK), P21 (sc- 6246, Santa Cruz Biotechnology, CA, USA), P53 (sc-126, Santa Cruz Biotechnology, CA, USA), and γ- H2AX (ab2893, Abcam, Cambridge, UK) . Secondary antibodies utilized were Donkey anti-Rabbit IgG (H+L) Highly Cross-Adsorbed Secondary Antibody, Alexa Fluor™ 488 (A-21206, Thermo Fisher Scientific, MA, USA), Donkey anti-Mouse IgG (H+L) Highly Cross-Adsorbed Secondary Antibody, Alexa Fluor™ 488 (A-21202, Thermo Fisher Scientific, MA, USA), Donkey anti-Rabbit IgG (H+L) Highly Cross-Adsorbed Secondary Antibody, Alexa Fluor™ 594 (A-21207, Thermo Fisher Scientific, MA, USA), and Donkey anti-Mouse IgG (H+L) Highly Cross-Adsorbed Secondary Antibody, Alexa Fluor™ 488 (A-21203, Thermo Fisher Scientific, MA, USA).

All images were captured using a fluorescent upright microscope (Olympus; BX43).

11. SA-β-gal assay

After washing with cold PBS, the RPE/choroid/scleral complex tissues were immediately fixed with the fixative solution provided in the SA- β- galactosidase (SA- β- gal) staining kit for 20 minutes at room temperature and then stained using the staining solution mix according to the manufacturer's protocol (BioVision, #K320, CA, USA). Following overnight SA- β- gal staining at 37 °C, the RPE/choroid/scleral complex tissues were depigmented by immersion in 10% H2O2 and incubated for 45 minutes on a 55 °C heat block. The tissues were then briefly rinsed with PBS and flat- mounted on slides for observation under an optical microscope.

All images were captured using a fluorescent upright microscope (Olympus; BX43).

12. Mouse Retinal Angiography and OCT

Following anesthesia, pupils were dilated, and mice were positioned on the Phoenix Micron IV (Phoenix MICRON, NY, USA) imaging platform. Fluorescein sodium was injected intraperitoneally for angiography, and retinal images were captured using the imaging system. Subsequently, OCT imaging was performed to acquire detailed cross-sectional scans of the retina. After the imaging procedure, mice were monitored during recovery from anesthesia and then returned to their habitat.

13. Electroretinography (ERG)

For the ERG procedure using the Celeris Electroretinography system (Diagnosys, MA, USA), mice were anesthetized and their pupils dilated with 1% tropicamide. The corneal surface was numbed using a topical anesthetic. During the procedure, the mice were placed on a heating pad. In the setup, a reference electrode was placed in the mouth, a ground electrode at the tail, and active electrodes on the cornea. The mice were dark-adapted overnight prior to the recordings. Scotopic ERG recordings were conducted at light intensities of 0.003, 0.01, 0.1, 1, 3, and 10 $cd.s/m^2$. Post-procedure, the mice were monitored until they recovered, and their eyes were treated with antibiotic ointment. The ERG waveforms were then analyzed to measure the a-wave and b-wave amplitudes at each light intensity.

14. Transcriptome analysis

Libraries for RNA-seq analysis were prepared according to the manufacturer's protocols with the NEBNext Ultra RNA Library Prep Kit. In brief, poly(T) magnetic beads attach to the oligo poly (A) to extract mRNA from the total RNA. Later, chemically fragmented mRNA was primed with random hexamer primers to synthesize the first-strand cDNA, from which the resulting fragments were then synthesized into double-strand cDNA. The product underwent end repair, A-tailing, and ligated to the sequencing adaptors. The library was selected with the AMPure XP beads and amplified through PCR. The prepared libraries were sequenced on the Illumina HiSeq 2500 platform to generate 150 bp paired-end reads. The sequencing quality controlled with FastQC is very high. Raw sequencing reads first went through the following pipeline: Trimmomatic was used to remove the adapters and long reads with low-quality bases. Later, the sequences were aligned to the reference genome by the STAR aligner. The expression levels of

the different genes were determined with feature counters. The DESeq2 package was used to check statistically differential gene expression between the treatments, considering all those with an FDR value up to 0.05. GO and KEGG pathway analyses were performed to provide a functional annotation and classification of the DEGs through the DAVID functional annotation tool.

15. Statistics

All group results are expressed as mean ± standard error of the mean (S.E.M.). Mean comparisons between groups were performed using the two-tailed Student's t-test or one-way ANOVA and Tukey post-hoc analyses for multiple groups. Statistical significance is denoted with *($P < 0.05$), **($P < 0.01$), ***($P < 0.001$) in the figures and figure legends. The statistical analyses were conducted using Prism software (GraphPad Prism, San Diego, CA, USA).

III. RESULTS

1. Optimization of Animal Model Conditions for Geographic Atrophy

Unlike the laser-induced CNV model commonly used for wet AMD, there have been no single dominant in vivo animal model for advanced dry AMD, geographic atrophy. Consequently, we aimed to use two distinct models: one induced by oxidative stress using sodium iodate and another through Alu RNA treatment. Given the variability in conditions reported in prior literature [55,56], we optimized the modeling conditions for further experiments.

The progression of dry AMD to geographic atrophy is naturally a chronic process; however, most AMD models artificially accelerate this process by imposing acute stress. This excessive stress can precipitate rapid cell death, which complicates the accurate evaluation of therapeutic effectiveness. To overcome this limitation, we sought to optimize the geographic atrophy model by modulating the dosage of the stress agent.

We determined the optimal concentration for disease modeling to be the dose at which RPE enlargement is observed prior to extensive cell death, at a designated time after the treatment of sodium iodate or Alu RNA. This approach facilitates a more refined evaluation of therapeutic interventions, more closely mimicking the slow progression characteristic of the disease.

Sodium iodate (NaIO3) was administered intravenously at three different doses in mice, and alterations in the Retinal Pigment Epithelium (RPE) were analyzed 7 days after administration (Figure 1A). At the low concentration of 15 mg/kg, no significant changes in the RPE were observed, whereas extensive RPE cell death was noted at the high concentration of 25 mg/kg. Consequently, a medium concentration of 20 mg/kg was determined to be optimal for modeling geographic atrophy, as it led to RPE enlargement without significant cell death (Fig.1B and Fig.1C).

Ambati group proposed that decreased DICER1 and increased Alu RNA lead to RPE degeneration via immunologic mechanisms and are the main pathogenesis of geographic atrophy.[58-60] Treatment of mouse retinas with transcribed Alu RNA mimicked the disease phenotype of dry AMD and the expression of cellular senescence-associated markers was induced.[21]

To visualize Alu RNA expression, we constructed a lentiviral vector co-expressing Alu RNA and GFP and in a similar context to the sodium iodate model, we optimized the lentivirus dose and analysis timing to achieve RPE enlargement without significant RPE cell death.

Prior to the delivery of Alu RNA, GFP expressing lentivirus was used to optimize the efficiency and toxicity of lentivirus transduction. When administered at three different concentrations, the transduction efficiency was significantly higher at 1.6*10^8 viral copies (vc)/μl compared to 0.8*10^8 vc/μl at 2 weeks post-injection (transduction efficiency: 62.99% ± 1.669 vs. 79.54 ± 2.241 %, $p<0.001$). However, at the higher concentration of 3.2*10^8 vc/μl, no additional increase in transduction efficiency was observed, and RPE enlargement indicating toxicity was detected (Fig.2A and Fig.2B).

Based on these results, we conducted future subretinal injection experiments using a concentration of 1.6*10^8 viral copies (vc)/μl.

Under a fixed viral concentration, we observed RPE morphology at 1, 2, and 4 weeks post-subretinal injection of GFP-lentivirus and AluRNA/GFP-lentivirus. In the case of GFP, no RPE degeneration was observed until 4 weeks, However, for AluRNA/GFP, a significant decrease in RPE cell count and morphological enlargement and irregularity were observed at 2 weeks (RPE cell count: 2673 ± 125 vs. 1829 ± 159, $p=0.01$) (Fig.2C and Fig.2D). Overall RPE cell death was observed at 4 weeks, with no cells expressing GFP. We determined that the 2-week time point post-Alu RNA transduction was appropriate for further analysis.

Further examination of the degenerated RPE region revealed an expansion of the affected area in the Alu group compared to the GFP control (Degeneration area: 1.089 ± 0.126 % vs. 23.55 ± 2.527 %, p<0.001) (Fig. 2E and 2F).

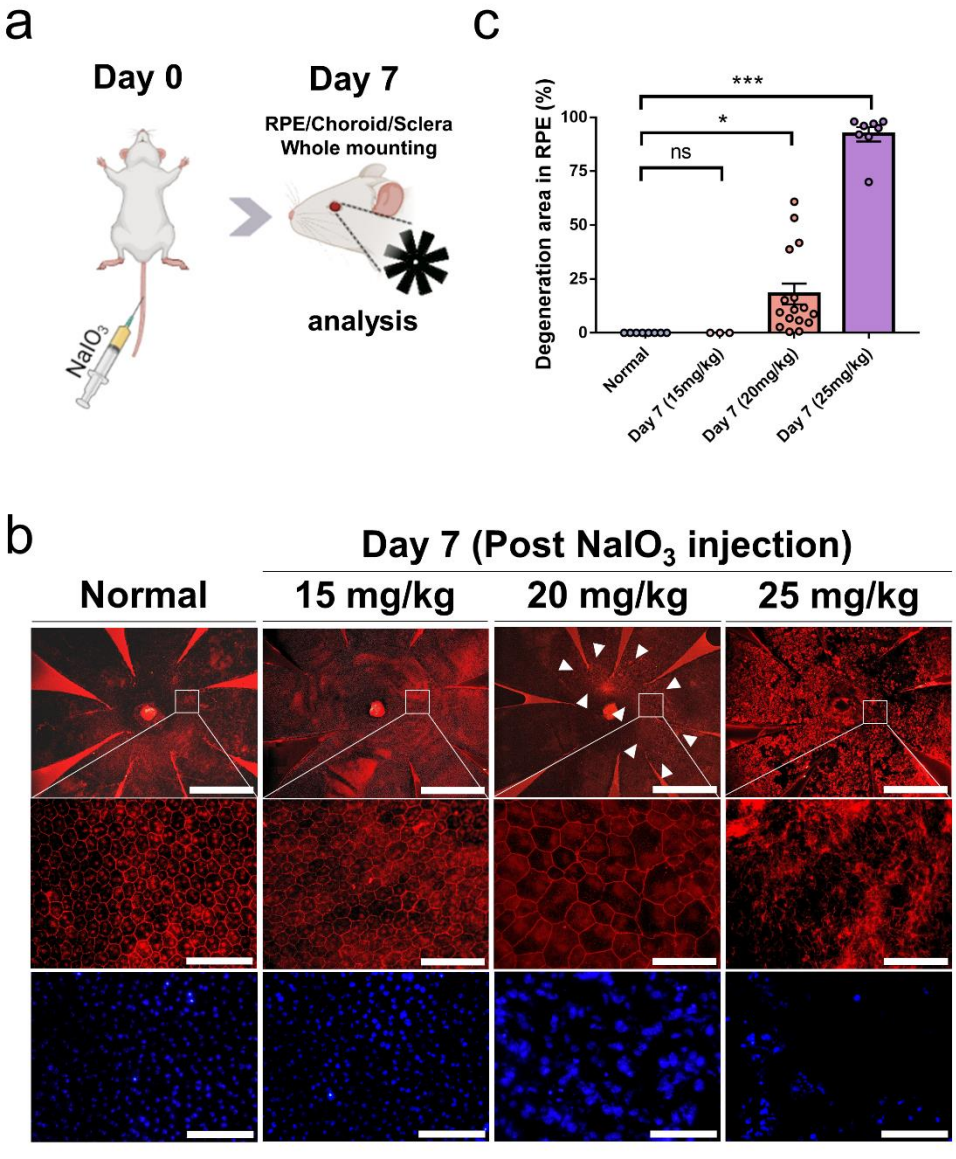

Figure 1. Phenotypic Characterization of RPE Cells in Mice Following NaIO3 Treatment. a.

Mice received NaIO3 intravenously through the tail vein, with evaluations performed 7 days post-t reatment. **b.** Phenotypic analysis of RPE cells post Zo-1 staining on whole mounts of RPE/choroid /sclera. Depicts overall retinal area with degenerative lesions (top row), RPE cell changes within le sions (middle row), and DAPI-positive nuclear alterations in lesions (bottom row). Scale bars: 1 m m (top row), 0.1 mm (middle and bottom rows). **c.** Proportion of atrophic areas relative to the total retina, indicating significant increase at higher doses (Control vs Day 7 (20mg/kg) $p=0.03$; (25mg/ kg) $p<0.001$).

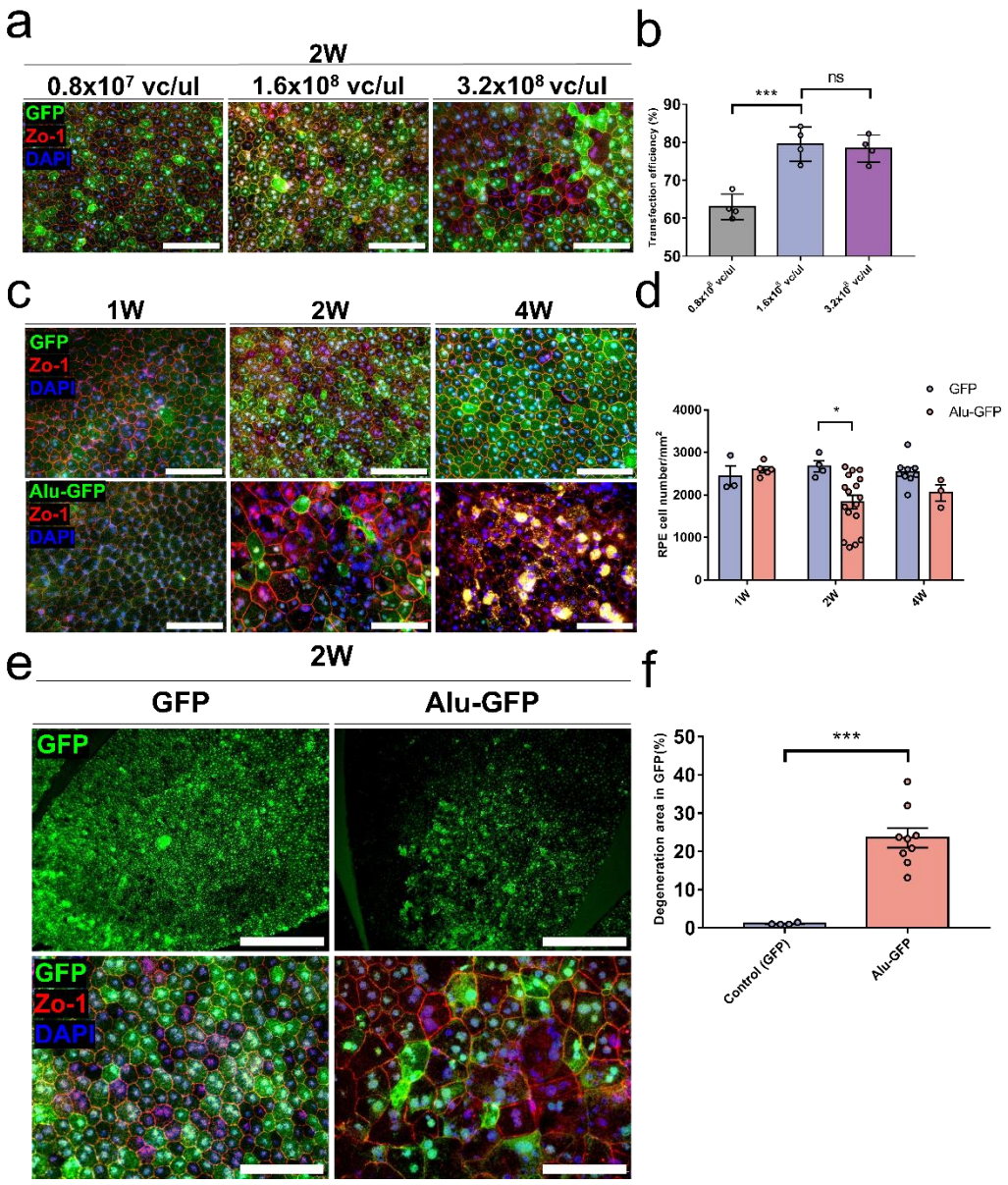

Figure 2. Investigating the Role of Alu RNA in Dry Age-Related Macular Degeneration via L enti-Viral Transfection. a. Visualization of GFP expression in RPE cells following transfection w ith lenti-virus at three varying concentrations, demonstrating the baseline transfection efficiency. S cale bar = 0.1mm. **b.** Examination of transfection efficiency in two weeks post-transfection with le

nti GFP, showing significantly higher at 1.6*10^8 viral copies (vc)/μl compared to 0.8*10^8 vc/μl (transduction efficiency: 62.99% ± 1.669 vs. 79.54 ± 2.241 %, p<0.001). At the higher concentrati on of 3.2*10^8 vc/μl, no additional increase in transduction efficiency was observed (transduction efficiency: 79.54 ± 2.241 % vs. 78.31 ± 1.783 %, p=0.89), and RPE enlargement indicating toxicit y was detected. **c and d**. Temporal analysis of RPE changes over 1, 2 and 4 weeks post-transfectio n with either lenti-GFP or lenti-Alu-GFP at a concentration of 1.6x10^8/1μl. The study tracks the p rogression of cellular changes indicative of degeneration. Scale bar = 0.1mm. (2W RPE cell count: 2673 ± 125 vs. 1829 ± 159, p=0.01) **e.** Detailed imaging reveals the overall RPE la yer, with highlighted areas of GFP transfection showing degeneration of RPE cells within the regio ns expressing Alu-GFP. Enlargement of RPE cells and nuclei, along with the loss of their hexagona l shape post Alu-GFP transfection, underscores the cytotoxic impact. Scale bar = 0.1mm. **f.** Quantif ication of degenerating RPE areas, using GFP expression as a reference, shows that Alu-GFP trans fection leads to significantly larger areas of degeneration compared to GFP control. (Degeneration area: 0.01 ± 0.001 % vs. 0.23 ± 0.025 %, p<0.001)

2. NAD+ level and expression of senescence marker in in vivo AMD models

When NMN was systemically administered to B6 mice, the NAD+ levels in the RPE/choroid/sclera complex significantly increased 142.3 ± 7.036% (p<0.001) (Fig. 3A). The NAD+ levels in the RPE/choroid/sclera complex were significantly reduced in the NaIO3-induced dry AMD model and the laser-induced CNV model compared to wild-type C57BL/6J (B6) mice (B6 vs. NaIO3, p=0.005; B6 vs. CNV, p=0.02) (Fig. 3B).

Senescence-Associated β-Galactosidase (SA-β-GAL) staining, a representative marker of cellular senescence, was performed in the RPE of 8-week-old wild-type B6 mice and the same age of NaIO3-induced dry AMD model and laser-induced CNV model, and significantly increased SA-β-GAL staining was observed in both disease models. In the NaIO3-induced dry AMD model, the staining was primarily detected in the mid-peripheral area where RPE degeneration mainly occurs and in the surrounding peripheral regions. In the CNV model, the staining was more intense around the CNV lesion along with the overall staining (Fig. 3C).

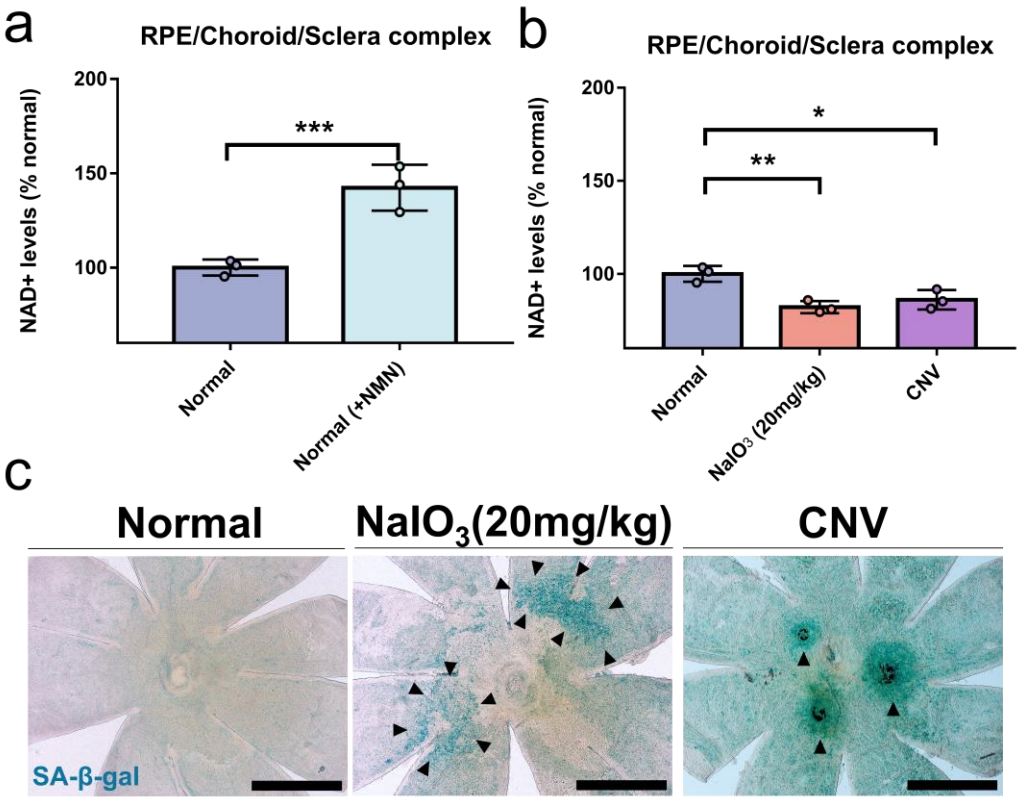

Figure 3. NAD+ Levels and Senescence in Retinal Models. a and b. Quantification of total NAD+ levels in the RPE/choroid/sclera complex from six eyeballs across three mice under conditions including: normal, NMN systemic injection, NaIO3 treatment, and CNV model. Significant increases in total NAD+ levels were observed in NMN-treated mice ($p < 0.001$), whereas NaIO3 (20mg/kg) led to decreased NAD+ levels ($p = 0.005$), and the CNV model showed reduced NAD+ levels ($p = 0.02$). **c.** SA-β-GAL staining in the RPE from normal, NaIO3, and CNV models displayed positive expression in senescence RPE cells. Scale bar=1mm.

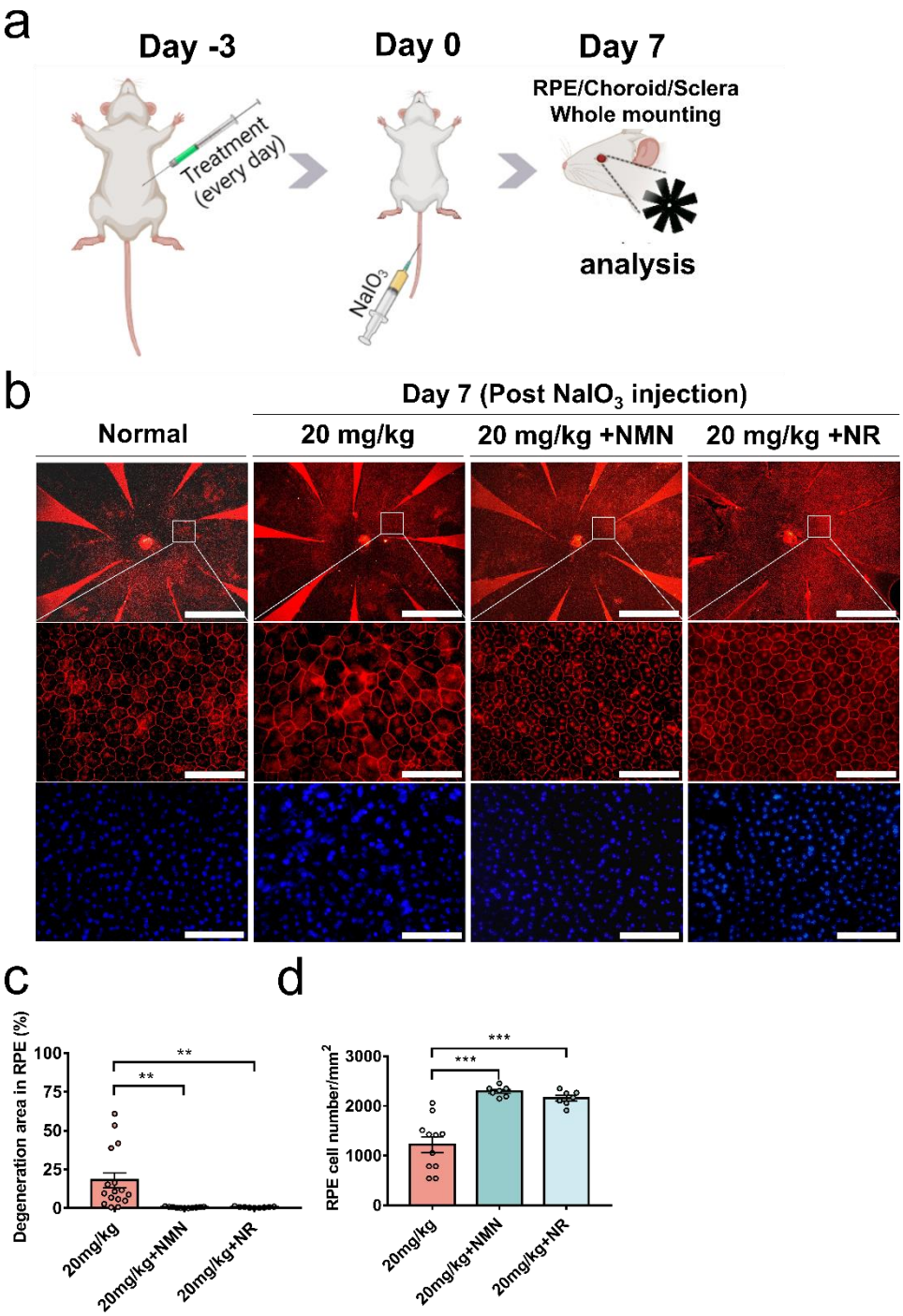

e

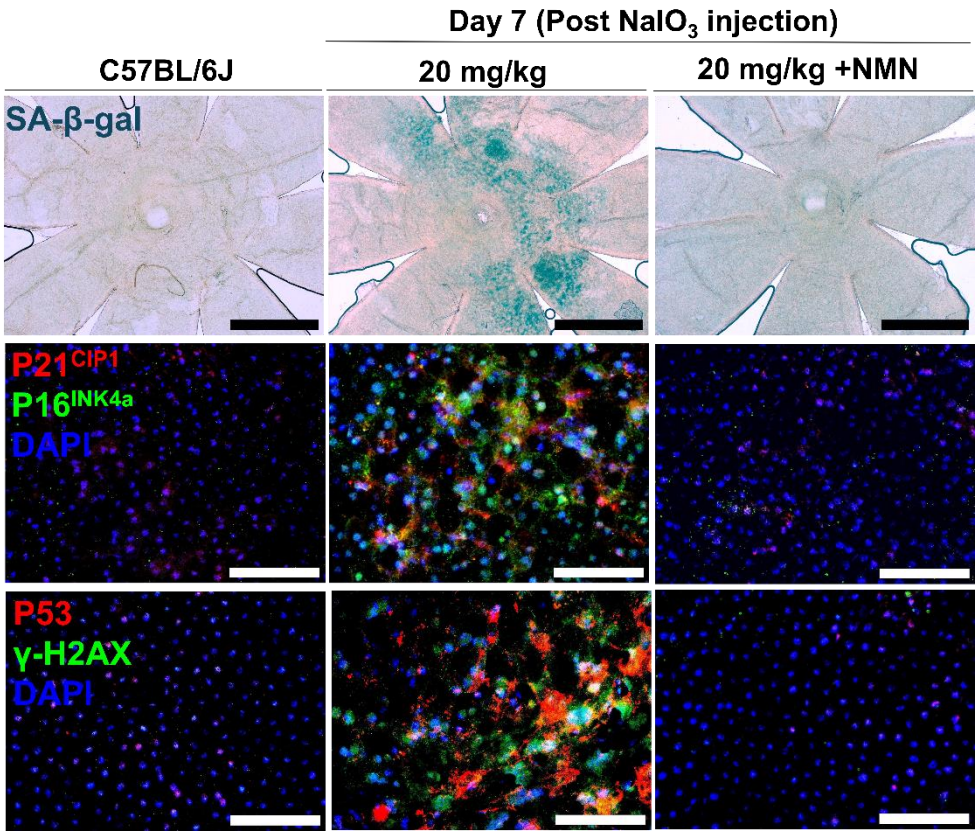

Figure 4. Impact of NMN and NR Treatment on NaIO3-Induced Retinal Degeneration in Mice. a. Mice received intraperitoneal injections of NMN or NR three days prior to NaIO3 administration (20mg/kg), with assessments conducted on Day 7 post-modeling. **b.** Phenotypic analysis via Zo-1 staining on whole mounts from normal C57BL/6J mice, the 20mg/kg NaIO3 model group, and the NMN and NR treatment groups. The first row shows the atrophic areas as a proportion of the total retina across groups. The second and third rows detail RPE cell changes and nuclear size variations, respectively, with enlarged views for clarity. Scale bars: 1 mm (top row), 0.1 mm (middle and bottom rows). **c.** Quantification of degenerative lesion areas relative to the total retina, demonstrating significant reductions with NMN (0.5 ± 0.12 %, p=0.005) and NR (0.65 ± 0.13 %, p=0.009) treatments compared to the model group. **d.** Comparison of RPE cell counts reveals significant increases with NMN (2296 ± 40, p<0.001) and NR (0.65 ± 0.13 %, p=0.009) treatments. **e.** SA-β-GA

L staining indicates senescence in the degeneration area of the 20mg/kg group, akin to the normal control, while the NMN treatment group exhibits no positive staining, suggesting reduced cellular senescence. Scale bar = 1mm. Co-expression of P21 and P16 in RPE cells within the 20mg/kg gro up signifies heightened senescence, which is notably absent in the NMN treatment and normal gro ups. Scale bar = 0.1mm. The 20mg/kg group shows positive expression of P53 and γ-H2AX in RP E cells, markers of cellular stress and senescence, unlike the NMN and normal groups which show negative expression. Scale bar = 0.1mm.

3. NAD+ precursors ameliorate the disease phenotypes and the associated senescence phenotypes in the dry AMD model.

In the Sodium Iodate-induced dry AMD model, NAD+ precursors NMN and NR were administered daily via intraperitoneal injection, starting three days prior to induction with Sodium Iodate and continuing until one week after the induction (Fig. 4A). Observations of the RPE morphology through RPE whole mounting one week after induction revealed that Sodium Iodate-induced RPE degeneration, characterized by enlargement and irregularity, was normalized by both NAD+ precurosrs (Fig. 4B). The area of degenerated RPE was significantly reduced in the NMN and NR treated groups (y and z, respectively), showing no significant difference from normal mice. (vs. Disease model; NMN, 0.5 ± 0.12 %, p=0.005; NR, 0.65 ± 0.13 %, p=0.009). Additionally, the number of RPE cells in the disease model mice was significantly higher in the NMN and NR treated groups (y and z, respectively) compared to the disease model (x), with no significant difference from normal mice. (vs. Disease model; NMN, 2296 ± 40, p<0.001; NR, 2159 ± 56, p<0.001) (Fig. 4C and Fig. 4D). The expression of cellular senescence markers, SA-β-GAL, P21^CIP1, P16^INK4a, P53, and γ-H2AX, which were elevated by Sodium Iodate, were dramatically normalized by NMN treatment (Fig. 4E).

In the retinal histology, attenuation and discontinuation of the RPE line were observed in the Sodium Iodate disease model and these pathologic features were ameliorated by NAD+ precursors. The thinning of the outer nuclear layer and total retinal thickness induced by Sodium Iodate was significantly increased by NMN and NR treatment (y and z, respectively), comparable to the thickness observed in normal mice (ONL: vs. Disease model; NMN, 44.28 ± 0.88 μm, p=0.03; NR, 42.96 ± 2.26 μm, p=0.04) (Total retina: vs. Disease model; NMN, 206.4 ± 4.90 μm,

p=0.04; NR, 212.4 ± 9.88 μm, p=0.02) (Fig. 5B and 5C).

Functionally, the ERG waveform was markedly flattened by sodium iodate treatment. The NMN treatment significantly increased the amplitude of the b-wave and a-wave at flash intensities of -1 log cd.s/m² and above, although it did not fully restore normal function observed in normal mice (Fig. 5D, Fig.5E and Fig. 5F).

Overall, NAD+ precursor treatment leads to structural improvement of the damaged RPE and neural retina, as well as functional recovery of visual function in a sodium iodate induced dry AMD model, which is accompanied by the amelioration of cellular senescence markers.

The effects of NAD+ precursors were also tested in another dry AMD model, the Alu-induced model. Subretinal injections were performed under the previously optimized conditions, and NAD+ precursor supplementation was systemically administered daily from 3 days prior to injection until 2 weeks, with analysis performed at 2 weeks (Fig. 6A). As a result, NMN and NR treatments significantly normalized the area of degenerated retina (Fig 6B and Fig6C) (vs. Alu, 26.8 ± 3.961 %, NMN, 4.887 ± 0.985 %, p<0.001; NR, 8.715 ± 1.399 %, p<0.001) and RPE cell count (Fig. 6D) (vs. Alu, 1829 ± 159, NMN, 2498 ± 130, p<0.001; NR, 2461 ± 94, p<0.001). OCT imaging confirmed the presence of degenerative area in the Alu group, while the NMN and NR groups exhibited substantial improvements (Fig. 6B)

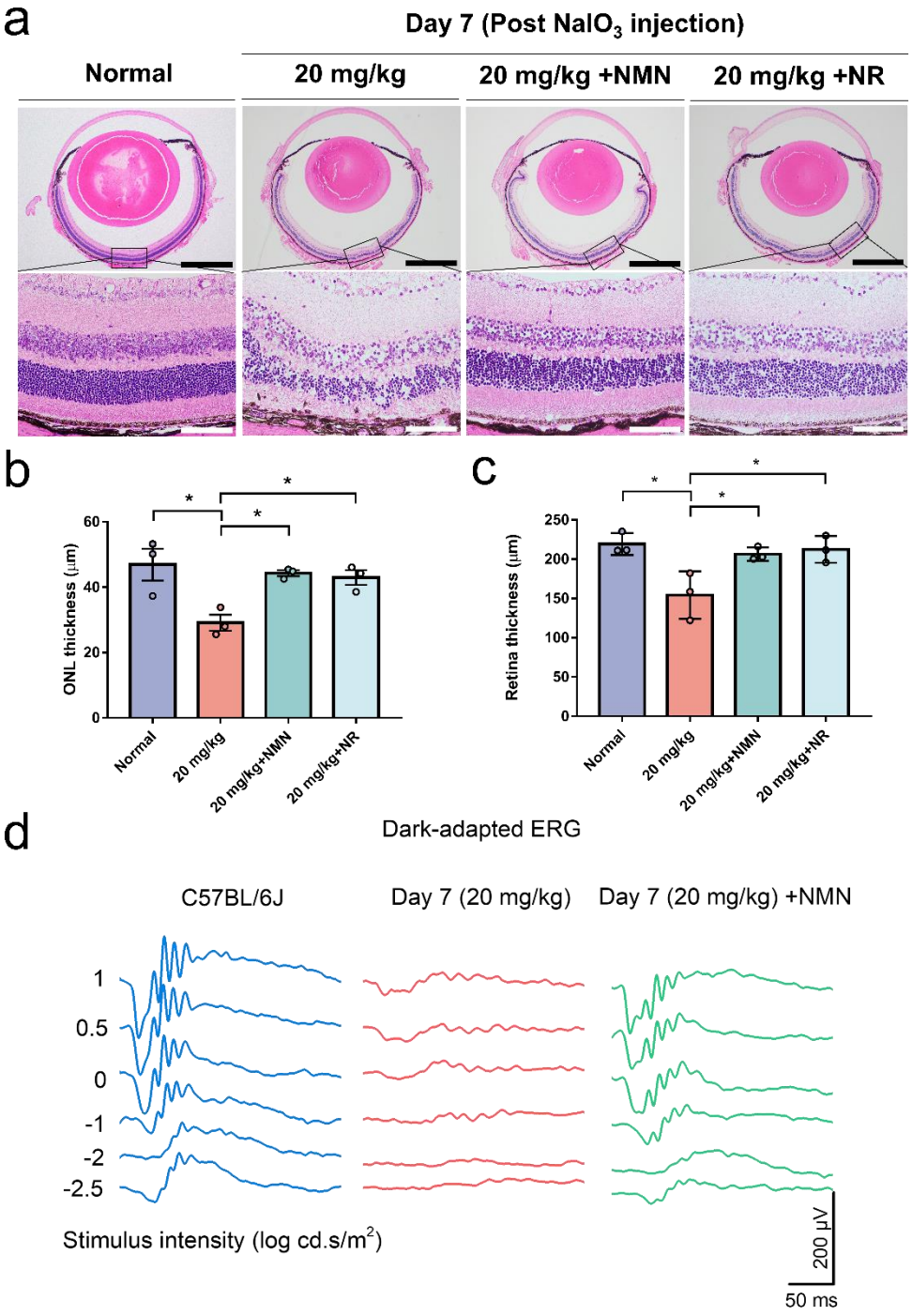

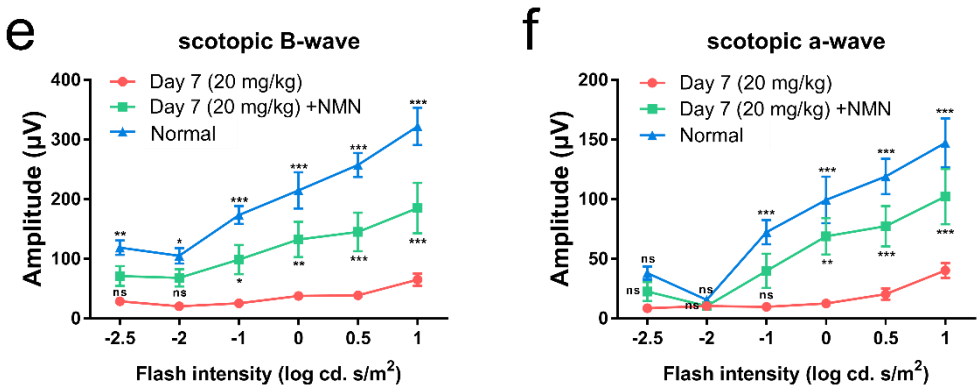

Figure 5. Comparative Analysis of Retinal Structure and Function in Mouse Models Post-Treatment. a. High-resolution imaging and H&E staining showcase retinal morphology across groups. The 20mg/kg NaIO3 group exhibits RPE degeneration and reactive retinal changes. Conversely, control, NMN, and NR treatment groups maintain normal RPE structure. Scale bars: 1 mm (overview), 0.1 mm (detailed views). **b.** Analysis of retinal and outer nuclear layer (ONL) thickness demonstrates significant ONL thinning in the 20mg/kg group, with NMN and NR treatments showing notable improvement towards normal thickness (C57BL/6J vs 20mg/kg p=0.01; 20mg/kg vs NMN p=0.03; 20mg/kg vs NR p=0.04). **c.** Overall retinal thickness comparisons across groups reveal no significant differences, suggesting selective ONL vulnerability (C57BL/6J vs 20mg/kg p=0.25; 20mg/kg vs NMN p=0.29; 20mg/kg vs NR p=0.21). **d-e.** Electrophysiological assessments via ERG under dark adaptation conditions. B-wave amplitude comparisons indicate significant impairment in the 20mg/kg group, with NMN treatment partially restoring function (C57BL/6J vs 20mg/kg, p<0.001 at -1 to 1 intensity; 20mg/kg vs NMN, p<0.001 at 0.5/1 intensity). **f.** A-wave response analysis further supports functional deterioration in the 20mg/kg group, with NMN treatment showing efficacy in functional recovery at higher intensities (C57BL/6J vs 20mg/kg, p<0.001 at -1 to 1 intensity; 20mg/kg vs NMN, p<0.001 at 0.5/1 intensity).

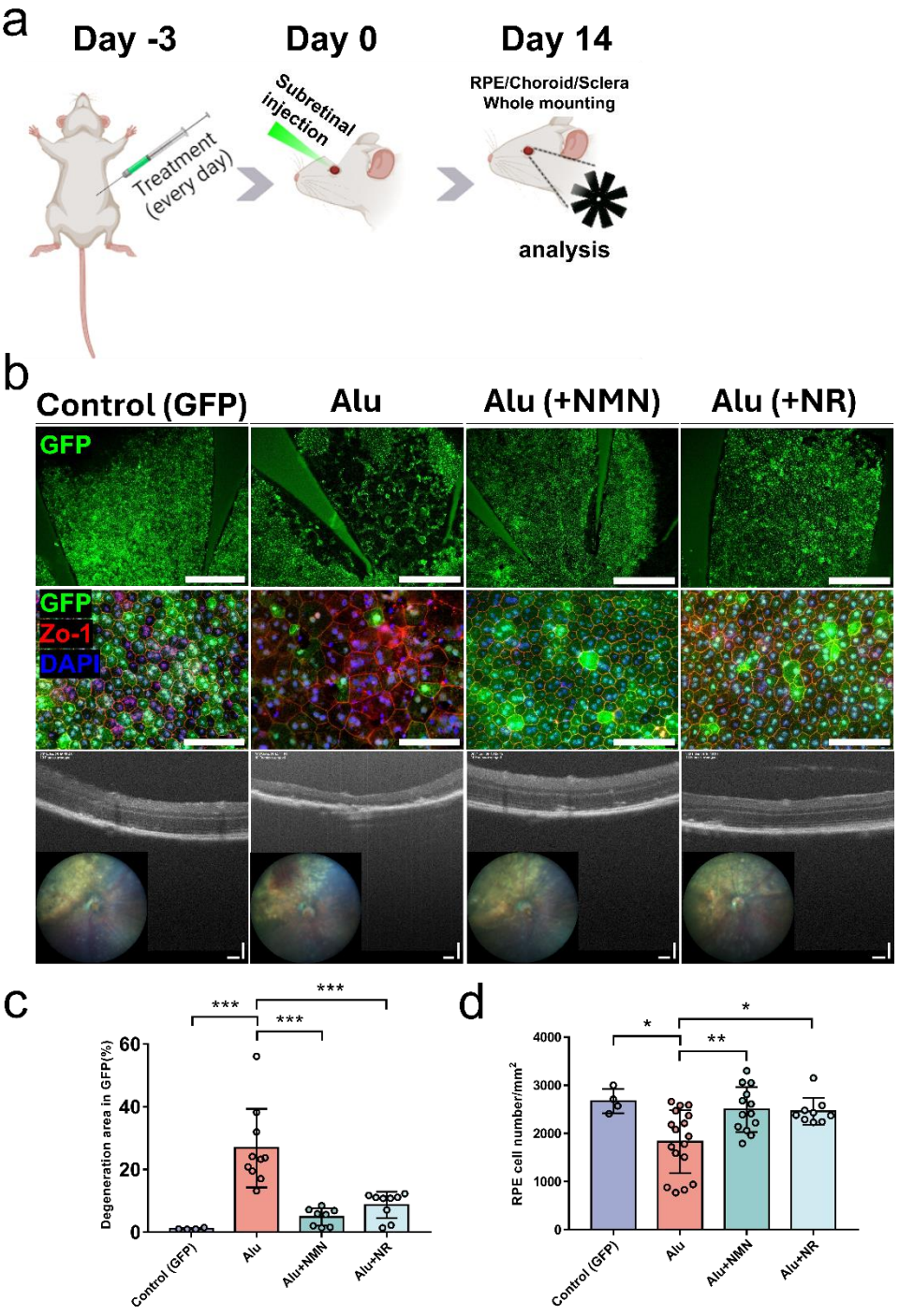

Figure 6. Therapeutic Effects of NMN and NR on Alu RNA-Induced Dry Age-Related Macular Degeneration. a. NAD+ precursor supplementation was systemically administered daily from 3 days prior to injection until 2 weeks, with analysis performed at 2 weeks **b.** Wide-ranging degeneration areas in the retinal pigment epithelium (RPE) are evident in the Alu-GFP group, with noticeable improvement observed in the NMN and NR treatment groups compared to Alu-GFP. Scale bar = 0.4mm. High-magnification images highlight the phenotypic improvements in RPE cells in the NMN and NR treatment groups compared to the Alu group. Scale bar = 0.1mm. Optical coherence tomography (OCT) and fundus imaging reveal neurosensory retina thinning of the Alu group, with significant improvement observed in the NMN and NR treatment groups. Scale bar = 0.1mm. **c.** Reduced degeneration areas are observed in the NMN and NR treatment groups compared to the Alu group (vs. Alu, 0.268 ± 0.04 %, Control (GFP),0.01 ± 0.001 %, $p<0.001$; NMN, 0.05 ± 0.01 %, $p<0.001$; NR, 0.09 ± 0.01 %, $p<0.001$). **d.** Increased RPE cell numbers are noted in the NMN and NR treatment groups compared to the Alu group (vs. Alu, Control (GFP), p=0.03; Alu+NMN p=0.006; Alu+NR p=0.03) (n=4-17).

4. Transcriptome Analysis of the Therapeutic Effects of NAD+ Supplementation

RNA sequencing analysis was performed to compare the gene expression profiles of RPE cells from normal control (B6 mice), dry AMD model (induced by Sodium Iodate, referred to as SI), and NMN-treated SI models. (Fig.7) We identified 999 genes significantly upregulated, and 183 genes downregulated in the SI group compared to the control, indicating a profound alteration in gene expression due to the dry AMD model induction. Notably, NMN treatment resulted in significant modulation of these expression changes.

NMN treatment notably reversed the expression of genes critical for visual system development and photoreceptor cell function, such as Abca4, Rdh5, Stra6, Mtor, Lrit3, Mfrp, Gabrr2, Clcn2, Slc24a1, Rpgrip1, Pde6c, Rd3, Nxnl1, Aanat, Nog, Pde8b, Nphp4, Gpr179, Vegfa, Bmp7, and Sipa1l3. These genes are essential for maintaining RPE and photoreceptor health, implicating NMN's role in preserving visual function in the context of AMD.

Functional enrichment analysis revealed that upregulated genes in the SI vs. control comparison were significantly enriched in pathways related to immune response, leukocyte

migration, and cytokine signaling, which are indicative of the inflammatory response associated with AMD. Conversely, NMN-treated samples showed a significant downregulation of these pathways, suggesting a reduction in inflammatory responses.

Notably, genes involved in visual system development and response to light stimulus, such as Per3, Cacna1c, Per2, and Asic2, were significantly downregulated in the dry AMD model but showed normalized expression levels upon NMN treatment, highlighting NMN's potential to maintain or restore visual function.

These results underscore the potential of NMN to counteract the deleterious effects of dry AMD on RPE cells by modulating gene expression associated with aging, inflammation, and visual system function. Our data provide compelling evidence that NMN treatment may represent a viable therapeutic strategy to mitigate RPE cell senescence, thereby preserving visual function in the context of AMD.

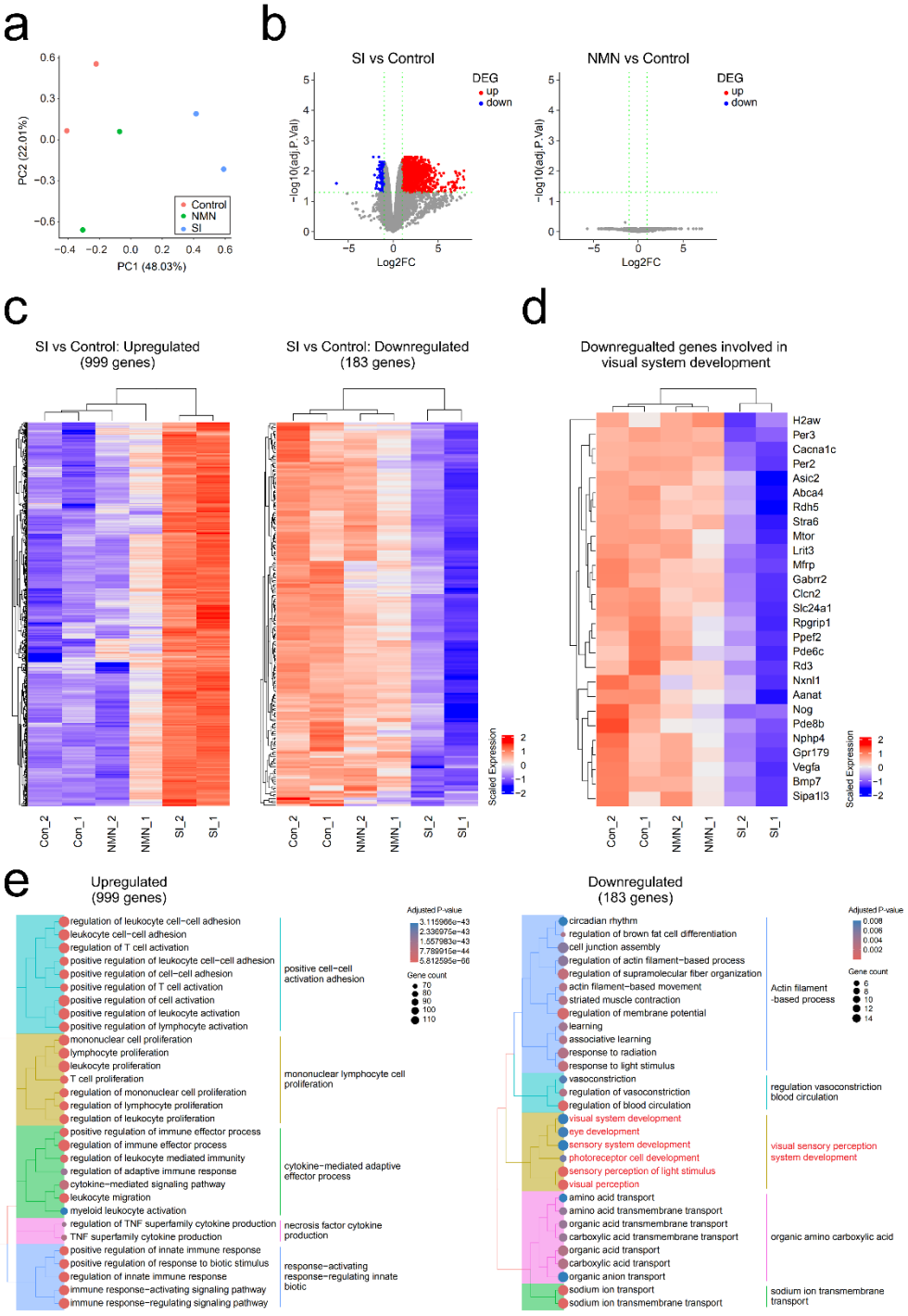

Figure 7. Overview of NMN Treatment Effects on Gene Expression. a. plots display the differential gene expression analysis for SI (sodium Iodate induced AMD) vs. Control and NMN vs. Control. The x-axis shows log2 fold change (Log2FC), and the y-axis shows -log10 of the adjusted p-value (adj.P.Val). Significant genes are colored, with upregulated in red and downregulated in blue. **b.** PCA plot shows the variance in gene expression profiles. Each point represents a sample, colored by group: Control (green), NMN (blue), and SI (red). PC1 and PC2 capture 48.03% and 22.01% of the variance, respectively. **c.** Heatmap displays scaled expression levels of differentially expressed genes across SI, NMN, and Control groups. Upregulated and downregulated genes are highlighted. **d.** Heatmap of downregulated genes involved in visual system development, such as Per3, Cacna1c, and Vegfa. The y-axis lists the genes, and the x-axis represents samples from Control, NMN, and SI groups, with color intensity indicating expression levels. **e.** Bar chart of top enriched GO terms for upregulated and downregulated genes in the SI vs. Control comparison. The x-axis shows gene count, and the y-axis lists GO terms related to immune response and visual perception. Adjusted p-values indicate significance.

5. NAD+ precursors significantly reduce laser-induced choroidal neovascularization

Localized senescent RPE cells were identified in NaIO3-induced retinal degeneration and laser-induced subretinal fibrosis mouse models [12]. In this study, we also identified senescent RPE cells surrounding the laser-induced CNV region (Fig 3C). Building on this discovery, we investigated the therapeutic effect of NAD+ precursors in mouse models of laser-induced CNV. NMN and NR were administered daily for three days prior to and seven days following the modeling of laser-induced choroidal neovascularization (CNV) (Fig.8A). As a positive control, intravitreal Aflibercept injection, which is currently the most widely used clinically, was used. The NMN and NR groups showed a significant reduction in CNV size compared to the control group, with values comparable to those in the Aflibercept group [vs. control, 17822 μm²; NMN, 8303 μm², $p<0.001$; NR, 9138 μm², $p<0.001$] [vs. Aflibercept, 8977 μm²; NMN, 8303 μm², $p>0.99$; NR, 8684 μm², $p>0.99$] (Fig.8B and Fig 8C). Induction of CNV at 3-4 sites around the optic nerve resulted in extensive SA-β-GAL staining across the retina and more intense staining around the CNV areas. NMN treatment significantly reduced overall retinal SA-β-GAL staining and decreased the intense staining around the CNV sites (Fig. 9A and Fig. 9B). The area of

cellular senescence markers expression, P21^CIP1, P16^INK4a, P53, and γ-H2AX, which were induced by laser induced CNV, were significantly reduced by NMN treatment (Fig.9C and Fig.9D).

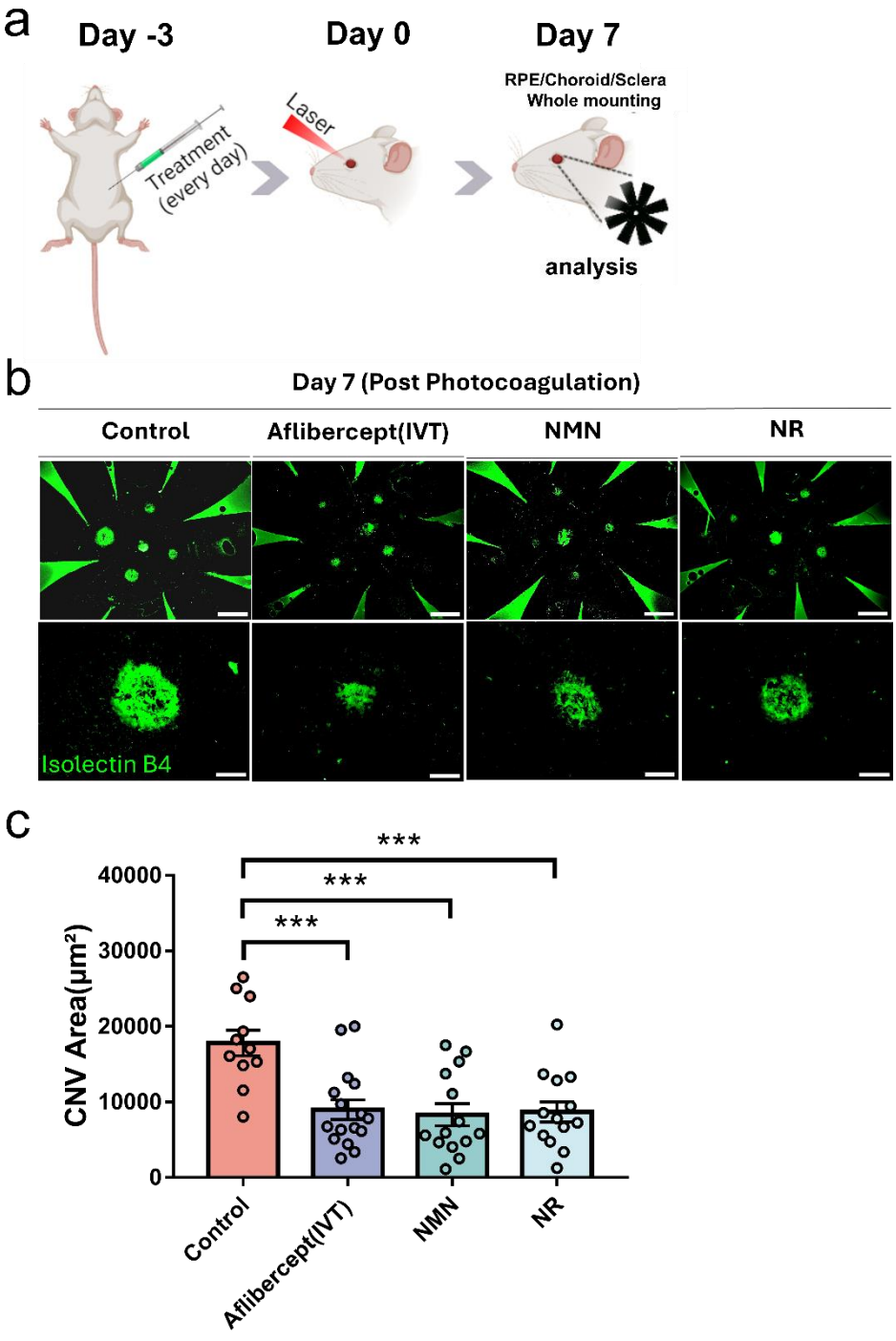

Figure 8. Evaluation of NMN and NR Treatment on Laser-Induced Choroidal Neovascularization (CNV). a. Treatment administered via intraperitoneal (IP) injection three days prior to CNV model creation. CNV lesions analyzed on Day 7 post-modeling. **b.** Isolectin B4 staining performed on RPE/choroid/sclera whole mounts. The top row displays the overall retina with CNV lesions (scale bar = 0.5mm), while the bottom row provides a high-magnification view of the CNV lesions (scale bar = 0.1mm). **c.** Comparison of CNV lesion sizes reveals smaller lesions in the Aflibercept (IVT), NMN, and NR treatment groups compared to the PBS-treated control (n=11-16; PBS vs Aflibercept (IVT) $p<0.001$; PBS vs NMN $p<0.001$; PBS vs NR $p<0.001$).

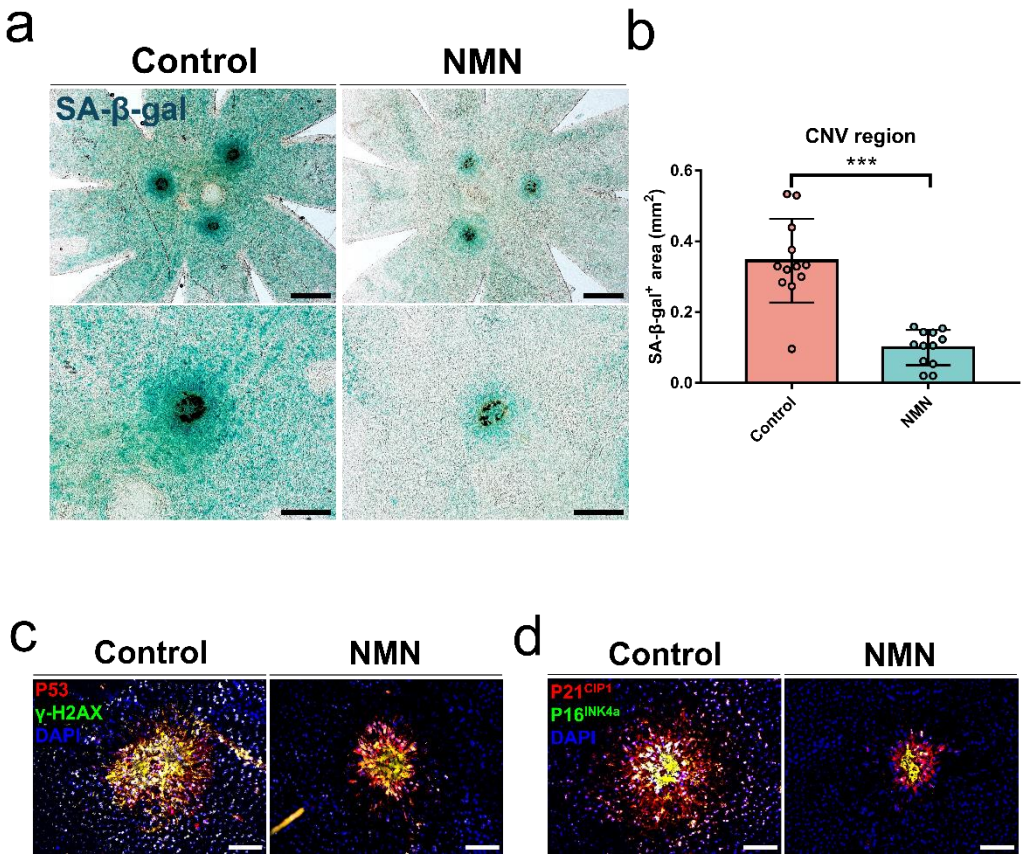

Figure 9. Senescence Phenotype Analysis in a Choroidal Neovascularization (CNV) Model and the Impact of NMN Treatment. a. SA-β-gal analysis reveals positive expression in RPE cells within the laser lesion area treated with PBS, with reduced positivity following NMN treatment. Top: scale bar = 0.5mm, bottom: scale bar = 0.25mm. **b**. Quantitative analysis of SA-β-gal-positive areas in the CNV lesion vicinity. Decreased positivity rates in both areas after NMN treatment compared to the control group show statistical significance (PBS vs NMN, $p<0.001$ for CNV region). **c.** Expression of P53 and γ-H2AX identified in RPE cells around the CNV lesion treated with PBS, with reduced positivity rates in NMN-treated areas. scale bar = 0.1mm. **d.** P21 and P16 staining indicate enlarged RPE cells positive around the CNV lesion treated with PBS, with decreased positivity rates following NMN treatment. scale bar = 0.1mm.

6. NAD+ precursor reduces the expression of neovascular and SASP factors

Quantitative PCR was performed to assess the expression of neovascular and SASP factors in retinal tissue of the CNV model and the NMN-treated CNV model. As expected, the expression of factors associated with CNV formation, such as Vegf, Pdgf-bb, and Col1, was significantly elevated in the CNV group. Interestingly, NMN supplementation significantly reduced the expression of these factors. Additionally, NMN treatment led to a reduction in the expression of SASP factors involved in inflammation and tissue remodeling, such as Il-6, Il-1a, Mmp3, and Mmp13, than in the CNV tissue. However, no significant difference was observed in the expression of Il-1b. (Fig. 10)

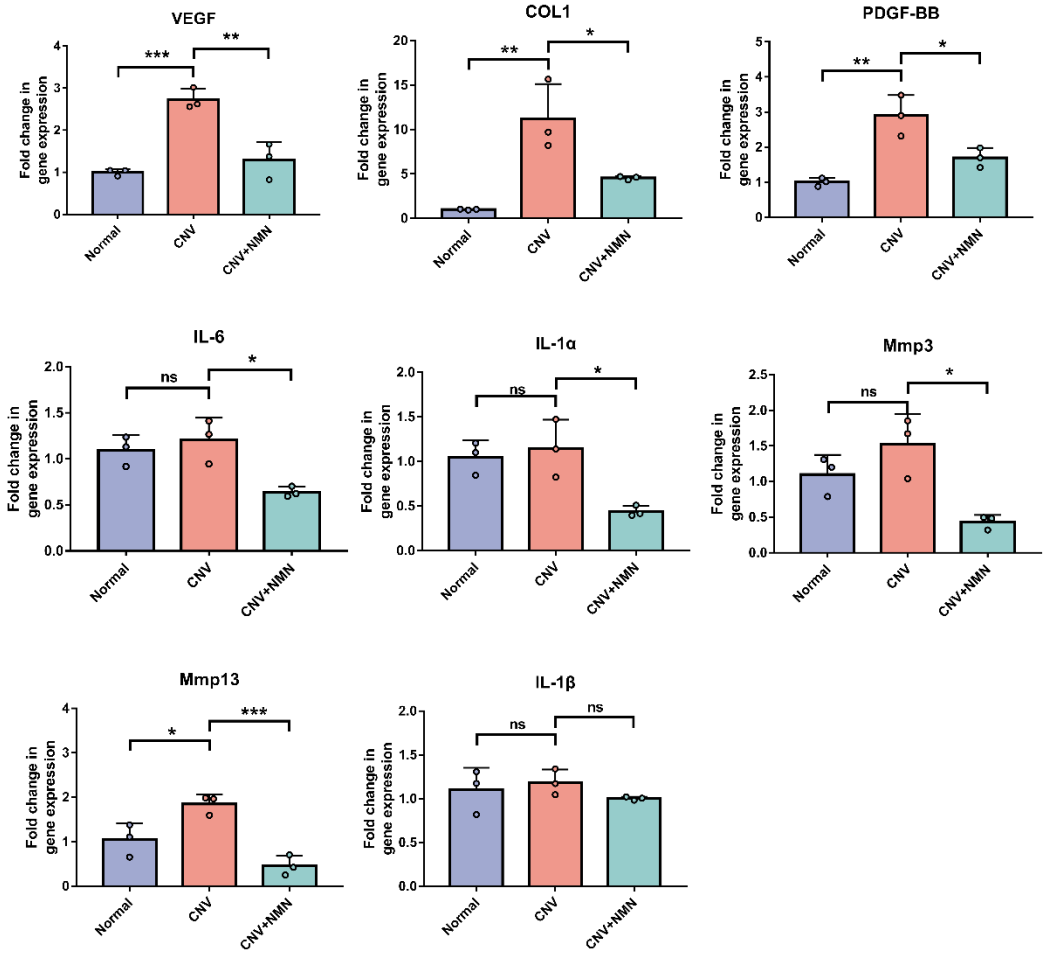

Figure 10. Real-Time PCR expression profiles of SASP-associated angiogenic and inflammatory biomarkers. VEGF is upregulated in CNV and reduced by NMN treatment (***p < 0.001, **p 0.003). COL1 shows increased levels in CNV, decreased with NMN (**p = 0.005, *p = 0.04). PDGF-BB is elevated in CNV and lessened by NMN (**p = 0.0026, *p = 0.0246). IL-6 expression is no significant change in CNV and decreased in NMN treated groups (p = 0.71, *p = 0.02). IL-1α expression is no significant change in CNV and decreased in NMN treated groups (p = 0.86, *p = 0.02). Mmp3 expression is no significant change in CNV and decreased in NMN treated groups (p = 0.40, *p = 0.01). Mmp13 is upregulated in CNV, mitigated by NMN (***p < 0.04, *p < 0.003). IL-1β remains unchanged (ns).

7. NAD+ precursors significantly reduce subsequent subretinal fibrosis

qPCR analysis demonstrated marked reduction in key fibrotic factors, such as Col1 and Pdgf-bb, in the NMN-treated group. Given that these factors are critical mediators of retinal fibrosis, their reduction suggests a potential mechanism through which NMN mitigates fibrotic processes, the biggest challenge of current treatment for wet AMD. During the treatment of wet AMD, subretinal fibrosis can occur despite repeated anti-VEGF injections, and this fibrosis is considered one of the primary causes of long-term vision loss. To assess the impact of NAD+ precursors on the fibrosis, we specifically analyzed the area of subretinal fibrosis at the fourth week post-laser induction, a time point previously established for evaluating the progression of the fibrosis in the CNV model. The formation of subretinal fibrosis at the fourth week post-laser induction as a mimic of subretinal scarring has been previously reported[12]. We found that at the fourth week post-laser induction, the subretinal scars marked by immunostaining for Collagen type 1 were significantly reduced in the NMN and NR treatment groups compared to the PBS group (vs. Control, 14394 μm^2 ; NMN, 6520 μm^2 , $p<0.001$; NR, 9890 μm^2 , $p=0.01$)(Fig.11A and Fig 11B). The subretinal fibrosis between the neural retina and RPE shows hyper-reflectivity on OCT and significantly reduced in the NMN treated group. Also, the immunohistochemistry shows a significant reduction of collagen type 1 positive subretinal scar in a representative cross section image (Fig.11C).

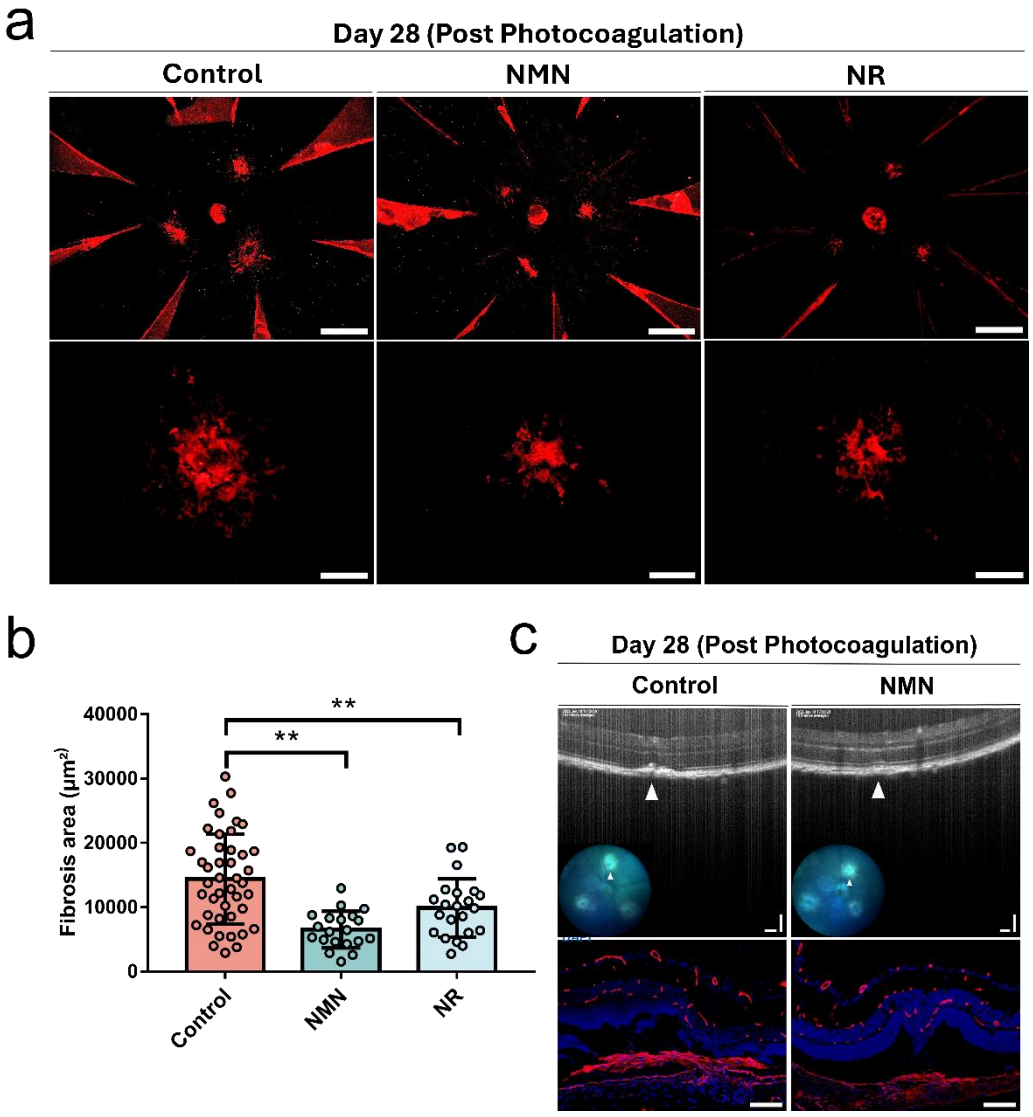

Figure 11. Comparison of Fibrosis Area in Laser-Induced CNV Model. a. On Day 28 post-laser induction, lesions treated with NMN and NR exhibited a significant reduction in Col-1 positive fibrosis area compared to the PBS group. Scale bar = 0.1mm**. b.** Statistical analysis demonstrates that the fibrosis area in lesions treated with NMN and NR was decreased compared to the PBS treatment group (n=23-44; NMN vs PBS p<0.001; NR vs PBS p=0.01). **c.** OCT imaging reveals high fluorescence reflection areas in the retinal pigment epithelium (RPE) and outer segment (OS) layers o

f the PBS group, while the RPE and OS layers appear more regular in the NMN group. Cross-secti onal Col-1 staining indicates that the Col-1 positive fibrosis beneath the neurosensory retina in the PBS-treated group was significantly larger than that in the NMN-treated group. Scale bar = 0.1mm.

IV. DISCUSSION

In this study, we elucidated the therapeutic potential of NAD+ supplementation across three established AMD mouse models, underscoring its capability to mitigate hallmark pathological features of both dry and wet AMD. Notably, our findings reveal that NAD+ supplementation can attenuate RPE degeneration and improve retinal function by modulating senescence-associated phenotypes. This is particularly relevant given the multifactorial nature of AMD, where cellular senescence and chronic inflammation play critical roles in disease progression.

Existing studies have demonstrated the therapeutic effects of NAD+ supplementation in mouse models of retinal degeneration.[34-36] In this paper, we further confirmed the specific senescence phenotype of RPE cells in three mouse AMD models, including markers such as SA-beta-gal, P21, p16, p53, H2ax, and SASP. Interestingly, in the AMD models, not only the lesion areas showed enhanced SA-beta-gal, but the surrounding RPE cells also exhibited. This indicates that not only the RPE cells in the degenerative regions but also the adjacent RPE cells accumulate and express senescence phenotypes, which is consistent with the progressive nature of AMD[59].

In the AMD models, measurements of NAD+ levels in RPE cells extracted from the lesion areas showed a significant decrease compared to normal RPE, consistent with the reduced NAD+ levels observed in human AMD. This provides supportive evidence for NAD+ supplementation as a beneficial treatment. The results also indicate that this treatment can improve senescence phenotypes and effectively enhance retinal structure and function in several mouse models.

In the RNA-seq analysis of NaIO3-induced mouse models, although there was no specific analysis of cellular senescence, the analysis of factors related to metabolism, immunity, and oxidative stress showed that NAD+ supplementation effectively improved the expression of these factors. It is well known that these factors are critical in senescent cells[24], indirectly

indicating that NAD+ therapy can improve RPE senescence phenotypes in NaIO3-induced mouse models.

Previously, Ambati et al. used 10% Neuroporter to transfect Alu RNA into subretinal RPE cells. To facilitate subsequent quantification of the degeneration area, we transfected a lentivirus expressing both Alu RNA and eGFP into subretinal RPE cells of mice. GFP expression clearly marks the regions transfected by the lentivirus, and when Alu is simultaneously expressed, the RPE cells exhibit degenerative changes.

Although this study does not further empirically demonstrate the relationship between NAD+ supplementation and SASP, numerous reports already suggest such an association[40]. When treated with NAD+ supplementation, effectively reducing macrophage activity and aggregation, thus diminishing immune responses in the disease microenvironment[60]. Additionally, NAD+ has been shown to improve mitochondrial function, reducing stress responses, and enhancing cellular robustness, leading to improvements[38]. Further research is warranted to elucidate the precise molecular mechanisms by which NAD+ supplementation exerts its effects, including its interaction with specific pathways involved in AMD progression.

For the effective translation of these preclinical successes into clinical practice, it is imperative to delineate the specific biological processes and molecular pathways through which NAD+ modulates retinal cell senescence and the SASP, thereby illuminating its role in mitigating AMD pathology. Future investigations should focus on elucidating the precise molecular mechanisms by which NAD+ influences cellular aging processes and SASP components in AMD, potentially identifying biomarkers for NAD+ efficacy and AMD progression. NAD+ supplementation holds unique potential to augment current AMD therapies, offering a comprehensive approach that not only targets specific pathological processes but also enhances overall cellular health and resilience, particularly in the metabolically demanding retinal environment.

V. CONCLUSION

In conclusion, our study underscores the potential of NAD+ supplementation not just as a therapeutic strategy for AMD, but as a paradigm shift towards addressing the underlying cellular aging processes. This approach harbors significant implications for future AMD research and offers a novel pathway to enhance patient outcomes in this challenging disease landscape.

REFERENCES

1. Daniel E, Toth C, Grunwald J, et al. Risk Factors for Scarring in the Comparison of Age-related Macular Degeneration Treatments Trials (CATT). Invest Ophth Vis Sci 2013;54(15) (In English) (<Go to ISI>://WOS:000436232708218).
2. Wang Y, Grenell A, Zhong F, et al. Metabolic signature of the aging eye in mice. Neurobiol Aging 2018;71:223-233. (In English). DOI: 10.1016/j.neurobiolaging.2018.07.024.
3. Coleman HR, Chan CC, Ferris FL, 3rd, Chew EY. Age-related macular degeneration. Lancet 2008;372(9652):1835-45. DOI: 10.1016/S0140-6736(08)61759-6.
4. Ambati J, Fowler BJ. Mechanisms of age-related macular degeneration. Neuron 2012;75(1):26-39. DOI: 10.1016/j.neuron.2012.06.018.
5. Tomany SC, Wang JJ, Van Leeuwen R, et al. Risk factors for incident age-related macular degeneration: pooled findings from 3 continents. Ophthalmology 2004;111(7):1280-7. DOI: 10.1016/j.ophtha.2003.11.010.
6. Heier JS, Lad EM, Holz FG, et al. Pegcetacoplan for the treatment of geographic atrophy secondary to age-related macular degeneration (OAKS and DERBY): two multicentre, randomised, double-masked, sham-controlled, phase 3 trials. Lancet 2023;402(10411):1434-1448. DOI: 10.1016/S0140-6736(23)01520-9.
7. Group CR, Martin DF, Maguire MG, et al. Ranibizumab and bevacizumab for neovascular age-related macular degeneration. N Engl J Med 2011;364(20):1897-908. DOI: 10.1056/NEJMoa1102673.
8. Daniel E, Toth CA, Grunwald JE, et al. Risk of scar in the comparison of age-related macular degeneration treatments trials. Ophthalmology 2014;121(3):656-66. DOI: 10.1016/j.ophtha.2013.10.019.
9. Acosta JC, Banito A, Wuestefeld T, et al. A complex secretory program orchestrated by the inflammasome controls paracrine senescence. Nat Cell Biol 2013;15(8):978-90. DOI:

10.1038/ncb2784.
10. Cuollo L, Antonangeli F, Santoni A, Soriani A. The Senescence-Associated Secretory Phenotype (SASP) in the Challenging Future of Cancer Therapy and Age-Related Diseases. Biology (Basel) 2020;9(12). DOI: 10.3390/biology9120485.
11. Roh K, Noh J, Kim Y, et al. Lysosomal control of senescence and inflammation through cholesterol partitioning. Nat Metab 2023;5(3):398-413. DOI: 10.1038/s42255-023-00747-5.
12. Sun Y, Wang X, Liu T, Zhu X, Pan X. The multifaceted role of the SASP in atherosclerosis: from mechanisms to therapeutic opportunities. Cell Biosci 2022;12(1):74. DOI: 10.1186/s13578-022-00815-5.
13. Barnes PJ, Baker J, Donnelly LE. Cellular Senescence as a Mechanism and Target in Chronic Lung Diseases. Am J Respir Crit Care Med 2019;200(5):556-564. DOI: 10.1164/rccm.201810-1975TR.
14. Chinta SJ, Woods G, Rane A, Demaria M, Campisi J, Andersen JK. Cellular senescence and the aging brain. Exp Gerontol 2015;68:3-7. DOI: 10.1016/j.exger.2014.09.018.
15. Chae JB, Jang H, Son C, et al. Targeting senescent retinal pigment epithelial cells facilitates retinal regeneration in mouse models of age-related macular degeneration. Geroscience 2021;43(6):2809-2833. DOI: 10.1007/s11357-021-00457-4.
16. Lazzarini R, Nicolai M, Pirani V, Mariotti C, Di Primio R. Effects of senescent secretory phenotype acquisition on human retinal pigment epithelial stem cells. Aging (Albany NY) 2018;10(11):3173-3184. DOI: 10.18632/aging.101624.
17. Oubaha M, Miloudi K, Dejda A, et al. Senescence-associated secretory phenotype contributes to pathological angiogenesis in retinopathy. Sci Transl Med 2016;8(362):362ra144. DOI: 10.1126/scitranslmed.aaf9440.
18. Blasiak J, Pawlowska E, Sobczuk A, Szczepanska J, Kaarniranta K. The Aging Stress Response and Its Implication for AMD Pathogenesis. Int J Mol Sci 2020;21(22). DOI: 10.3390/ijms21228840.
19. Glotin AL, Debacq-Chainiaux F, Brossas JY, et al. Prematurely

senescent ARPE-19 cells display features of age-related macular degeneration. Free Radic Biol Med 2008;44(7):1348-61. DOI: 10.1016/j.freeradbiomed.2007.12.023.

20. Malek G, Campisi J, Kitazawa K, Webster C, Lakkaraju A, Skowronska-Krawczyk D. Does senescence play a role in age-related macular degeneration? Exp Eye Res 2022;225:109254. DOI: 10.1016/j.exer.2022.109254.
21. Marazita MC, Dugour A, Marquioni-Ramella MD, Figueroa JM, Suburo AM. Oxidative stress-induced premature senescence dysregulates VEGF and CFH expression in retinal pigment epithelial cells: Implications for Age-related Macular Degeneration. Redox Biol 2016;7:78-87. DOI: 10.1016/j.redox.2015.11.011.
22. Sreekumar PG, Reddy ST, Hinton DR, Kannan R. Mechanisms of RPE senescence and potential role of alphaB crystallin peptide as a senolytic agent in experimental AMD. Exp Eye Res 2022;215:108918. DOI: 10.1016/j.exer.2021.108918.
23. Chaib S, Tchkonia T, Kirkland JL. Cellular senescence and senolytics: the path to the clinic. Nat Med 2022;28(8):1556-1568. DOI: 10.1038/s41591-022-01923-y.
24. He S, Sharpless NE. Senescence in Health and Disease. Cell 2017;169(6):1000-1011. DOI: 10.1016/j.cell.2017.05.015.
25. Fletcher RS, Lavery GG. The emergence of the nicotinamide riboside kinases in the regulation of NAD+ metabolism. J Mol Endocrinol 2018;61(3):R107-R121. DOI: 10.1530/JME-18-0085.
26. Belenky P, Bogan KL, Brenner C. NAD+ metabolism in health and disease. Trends Biochem Sci 2007;32(1):12-9. DOI: 10.1016/j.tibs.2006.11.006.
27. Lin JB, Apte RS. NAD(+) and sirtuins in retinal degenerative diseases: A look at future therapies. Prog Retin Eye Res 2018;67:118-129. DOI: 10.1016/j.preteyeres.2018.06.002.
28. Lin JB, Kubota S, Ban N, et al. NAMPT-Mediated NAD(+) Biosynthesis Is Essential for Vision In Mice. Cell Rep 2016;17(1):69-85. DOI: 10.1016/j.celrep.2016.08.073.
29. Bai S, Sheline CT. NAD(+) maintenance attenuates light induced photoreceptor degeneration. Exp Eye Res 2013;108:76-83. DOI: 10.1016/j.exer.2012.12.007.

30. Tam D, Tam M, Maynard KI. Nicotinamide modulates energy utilization and improves functional recovery from ischemia in the in vitro rabbit retina. Ann N Y Acad Sci 2005;1053:258-68. DOI: 10.1196/annals.1344.023.
31. Sheline CT, Zhou Y, Bai S. Light-induced photoreceptor and RPE degeneration involve zinc toxicity and are attenuated by pyruvate, nicotinamide, or cyclic light. Mol Vis 2010;16:2639-52. (https://www.ncbi.nlm.nih.gov/pubmed/21179242).
32. Zhang M, Jiang N, Chu Y, et al. Dysregulated metabolic pathways in age-related macular degeneration. Sci Rep 2020;10(1):2464. DOI: 10.1038/s41598-020-59244-4.
33. Zabka TS, Singh J, Dhawan P, et al. Retinal toxicity, in vivo and in vitro, associated with inhibition of nicotinamide phosphoribosyltransferase. Toxicol Sci 2015;144(1):163-72. DOI: 10.1093/toxsci/kfu268.
34. Zhang X, Henneman NF, Girardot PE, et al. Systemic Treatment With Nicotinamide Riboside Is Protective in a Mouse Model of Light-Induced Retinal Degeneration. Invest Ophthalmol Vis Sci 2020;61(10):47. DOI: 10.1167/iovs.61.10.47.
35. Chen X, Amorim JA, Moustafa GA, et al. Neuroprotective effects and mechanisms of action of nicotinamide mononucleotide (NMN) in a photoreceptor degenerative model of retinal detachment. Aging (Albany NY) 2020;12(24):24504-24521. DOI: 10.18632/aging.202453.
36. Ren C, Hu C, Wu Y, et al. Nicotinamide Mononucleotide Ameliorates Cellular Senescence and Inflammation Caused by Sodium Iodate in RPE. Oxid Med Cell Longev 2022;2022:5961123. DOI: 10.1155/2022/5961123.
37. Verdin E. NAD(+) in aging, metabolism, and neurodegeneration. Science 2015;350(6265):1208-13. DOI: 10.1126/science.aac4854.
38. Katsyuba E, Romani M, Hofer D, Auwerx J. NAD(+) homeostasis in health and disease. Nat Metab 2020;2(1):9-31. DOI: 10.1038/s42255-019-0161-5.
39. Massudi H, Grant R, Braidy N, Guest J, Farnsworth B, Guillemin GJ. Age-Associated Changes In Oxidative Stress and NAD+ Metabolism In Human Tissue. PLOS ONE 2012;7(7):e42357. DOI:

10.1371/journal.pone.0042357.
40. Cerutti R, Pirinen E, Lamperti C, et al. NAD(+)-dependent activation of Sirt1 corrects the phenotype in a mouse model of mitochondrial disease. Cell Metab 2014;19(6):1042-9. DOI: 10.1016/j.cmet.2014.04.001.
41. Ralto KM, Rhee EP, Parikh SM. NAD(+) homeostasis in renal health and disease. Nat Rev Nephrol 2020;16(2):99-111. DOI: 10.1038/s41581-019-0216-6.
42. Covarrubias AJ, Kale A, Perrone R, et al. Senescent cells promote tissue NAD(+) decline during ageing via the activation of CD38(+) macrophages. Nat Metab 2020;2(11):1265-1283. DOI: 10.1038/s42255-020-00305-3.
43. Chini CCS, Cordeiro HS, Tran NLK, Chini EN. NAD metabolism: Role in senescence regulation and aging. Aging Cell 2024;23(1):e13920. DOI: 10.1111/acel.13920.
44. Frederick DW, Loro E, Liu L, et al. Loss of NAD Homeostasis Leads to Progressive and Reversible Degeneration of Skeletal Muscle. Cell Metab 2016;24(2):269-82. DOI: 10.1016/j.cmet.2016.07.005.
45. Gomes AP, Price NL, Ling AJ, et al. Declining NAD(+) induces a pseudohypoxic state disrupting nuclear-mitochondrial communication during aging. Cell 2013;155(7):1624-38. DOI: 10.1016/j.cell.2013.11.037.
46. Wiley CD, Velarde MC, Lecot P, et al. Mitochondrial Dysfunction Induces Senescence with a Distinct Secretory Phenotype. Cell Metab 2016;23(2):303-14. DOI: 10.1016/j.cmet.2015.11.011.
47. Mills KF, Yoshida S, Stein LR, et al. Long-Term Administration of Nicotinamide Mononucleotide Mitigates Age-Associated Physiological Decline in Mice. Cell Metab 2016;24(6):795-806. DOI: 10.1016/j.cmet.2016.09.013.
48. Yoshino J, Mills KF, Yoon MJ, Imai S. Nicotinamide mononucleotide, a key NAD(+) intermediate, treats the pathophysiology of diet- and age-induced diabetes in mice. Cell Metab 2011;14(4):528-36. DOI: 10.1016/j.cmet.2011.08.014.
49. Espinoza SE, Khosla S, Baur JA, de Cabo R, Musi N. Drugs Targeting Mechanisms of Aging to Delay Age-Related Disease and

Promote Healthspan: Proceedings of a National Institute on Aging Workshop. J Gerontol A Biol Sci Med Sci 2023;78(Suppl 1):53-60. DOI: 10.1093/gerona/glad034.

50. Sasaki L, Hamada Y, Yarimizu D, et al. Intracrine activity involving NAD-dependent circadian steroidogenic activity governs age-associated meibomian gland dysfunction. Nat Aging 2022;2(2):105-114. DOI: 10.1038/s43587-021-00167-8.
51. de Picciotto NE, Gano LB, Johnson LC, et al. Nicotinamide mononucleotide supplementation reverses vascular dysfunction and oxidative stress with aging in mice. Aging Cell 2016;15(3):522-30. DOI: 10.1111/acel.12461.
52. Ebeling MC, Polanco JR, Qu J, Tu C, Montezuma SR, Ferrington DA. Improving retinal mitochondrial function as a treatment for age-related macular degeneration. Redox Biol 2020;34:101552. DOI: 10.1016/j.redox.2020.101552.
53. Lin R, Yu J. The role of NAD(+) metabolism in macrophages in age-related macular degeneration. Mech Ageing Dev 2023;209:111755. DOI: 10.1016/j.mad.2022.111755.
54. Wang J, Iacovelli J, Spencer C, Saint-Geniez M. Direct effect of sodium iodate on neurosensory retina. Invest Ophthalmol Vis Sci 2014;55(3):1941-53. DOI: 10.1167/iovs.13-13075.
55. Tarau IS, Berlin A, Curcio CA, Ach T. The Cytoskeleton of the Retinal Pigment Epithelium: from Normal Aging to Age-Related Macular Degeneration. Int J Mol Sci 2019;20(14) (In English). DOI: 10.3390/ijms20143578.
56. Kaneko H, Dridi S, Tarallo V, et al. DICER1 deficit induces Alu RNA toxicity in age-related macular degeneration. Nature 2011;471(7338):325-330. (HTTP://sfx-82yum.hosted.exlibrisgroup.com/yum?sid=Entrez%3APubMed&id=pmid%3A21297615).
57. Tarallo V, Hirano Y, Gelfand BD, et al. DICER1 loss and Alu RNA induce age-related macular degeneration via the NLRP3 inflammasome and MyD88. Cell 2012;149(4):847-859. (HTTP://sfx-82yum.hosted.exlibrisgroup.com/yum?sid=Entrez%3APubMed&id=pmid%3A22541070).
58. Fukuda S, Narendran S, Varshney A, et al. Alu complementary DNA

is enriched in atrophic macular degeneration and triggers retinal pigmented epithelium toxicity via cytosolic innate immunity. Science Advances 2021;7(40):eabj3658-eabj3658. (HTTP://sfx-82yum.hosted.exlibrisgroup.com/yum?sid=Entrez%3APubMed&id=pmid%3A34586848).

59. Fleckenstein M, Schmitz-Valckenberg S, Chakravarthy U. Age-Related Macular Degeneration: A Review. JAMA 2024;331(2):147-157. DOI: 10.1001/jama.2023.26074.
60. Cameron AM, Castoldi A, Sanin DE, et al. Inflammatory macrophage dependence on NAD(+) salvage is a consequence of reactive oxygen species-mediated DNA damage. Nat Immunol 2019;20(4):420-432. DOI: 10.1038/s41590-019-0336-y.
61. Kerur N, Fukuda S, Banerjee D, et al. cGAS drives noncanonical-inflammasome activation in age-related macular degeneration. Nature Medicine 2018;24(1):50-61. DOI: 10.1038/nm.4450.
62. Park J, Cui G, Lee H, et al. CRISPR/Cas9 mediated specific ablation of vegfa in retinal pigment epithelium efficiently regresses choroidal neovascularization. Sci Rep 2023;13(1):3715. DOI: 10.1038/s41598-023-29014-z.
63. Ishikawa K, Sreekumar PG, Spee C, et al. alphaB-Crystallin Regulates Subretinal Fibrosis by Modulation of Epithelial-Mesenchymal Transition. Am J Pathol 2016;186(4):859-73. DOI: 10.1016/j.ajpath.2015.11.014.

Abstract in Korean

NAD+에 의한 망막색소상피세포 노화 억제로 나이 관련 황반변성 진행 완화의 효과성

나이 관련 황반변성(AMD)은 선진국에서 노인들 사이에서 실명의 주요 원인입니다. AMD는 건성과 습성 두 가지 유형으로 분류됩니다; 건성 AMD는 망막 색소 상피(RPE) 위축을 특징으로 하며 효과적인 치료법이 부족합니다. 습성 AMD는 맥락막 신생혈관증에서 기원하며 혈관내피 성장인자(VEGF)를 표적으로 하는 단클론 항체의 반복적인 안구 내 주사로 치료되지만, 장기적인 관찰을 통해 망막하 섬유화와 시력 악화로 진행되는 것이 확인되어, 충족되지 않은 치료 필요성을 나타냅니다. 노화와 함께, 인간의 세포 내 니코틴아미드 아데닌 디뉴클레오티드(NAD+) 수준은 망막을 포함하여 감소합니다. 수많은 연구들은 NAD+ 수준을 높이는 것의 항노화 효과와 노령 관련 질병에 대한 치료적 이점을 입증하였습니다. 본 연구에서, 우리는 건성 및 습성 AMD의 생체 내 모델에서 NAD+ 증가의 치료 효과를 조사하였습니다.

건성 AMD의 지리적 위축(GA) 모델과 습성 AMD의 레이저 유도 맥락막 신생혈관(CNV) 모델 모두에서 망막 내 세포 NAD+ 수준 감소 및 노화 표지자의 증가된 발현이 확인되었습니다.

니코틴아미드 모노뉴클레오타이드(NMN) 및 니코틴아미드 리보사이드(NR)와 같은 NAD+ 전구체의 체계적 보충은 망막 내 NAD+ 수준을 증가하였습니다. 생체 내 GA 모델에서, NAD+ 전구체는 RPE 위축을 유의하게 감소시켰고, 나이 관련 표지자의 발현을 감소시키며, 시각 기능을 향상시켰습니다. 전사체 분석은 NAD+ 전구체가 염증 관련 유전자 세트 발현을 줄이고 시각 시스템 관련 유전자 세트 발현을 증가시킨 것으로 나타냈습니다. 또한, NAD+ 전구체는 레이저 유도 CNV 모델에서 병변 크기를 현저하게 줄여, 현재 임상 개입인 안구 내 아플리버셉트와 비교할 수 있었습니다. 노화 표지자, 혈관 생성 인자, 및 노화 관련 분비 표현형(SASP)의 유전자 발현이 유의하게 감소하였습니다. 더욱이, 이 치료 전략은 망막하 섬유화 감소를 동시에

촉진하였습니다.

현재 다양한 질병을 치료하고 노화를 방지하기 위한 NAD+ 전구체의 효능을 탐색하기 위한 임상 시험이 진행 중이며, 이는 인간 사용에 안전한 것으로 간주됩니다. 우리의 전임상 모델에서 얻은 증거에 기반하여, NAD+ 전구체를 보충하는 것은 치료 옵션이 제한된 나이 관련 황반변성을 위한 새로운 치료 접근법으로 사용될 수 있습니다.

핵심되는 말: 연령 관련 황반변성, 노화, 니코티나마이드 아데닌 디뉴클레오티드